JOURNAL OF GEOPHYSICAL RESEARCH: SPACE PHYSICS, VOL. 118, 1–22, doi:10.1002/jgra.50188, 2013

Radio emissions from terrestrial gamma-ray flashes

Joseph R. Dwyer[1] and Steven A. Cummer[2]

Received 16 November 2012; revised 29 January 2013; accepted 12 February 2013.

[1] The theory of radio frequency (RF) emissions by terrestrial gamma-ray flashes (TGFs) is developed. These radio emissions, which are separate from the emission caused by lightning, are produced by the electric currents generated by runaway electrons and resulting low-energy electrons and ions. It is found from theory that the radio frequency pulses produced by TGFs are large enough to measure. Features of these signals depend strongly on certain aspects of the runaway acceleration process and so should provide additional information about the source mechanism(s) of this interesting atmospheric phenomenon. The RF emissions from several TGF models are calculated and compared with measurements of TGF-associated radio pulses, and it is found that the measured energy densities at higher frequencies support a source mechanism that involves a very large ($>10^4$) number of distinct seed particle injections. In particular, the results are consistent with the relativistic feedback discharge model of TGFs.

Citation: Dwyer, J. R., and S. A. Cummer (2013), Radio emissions from terrestrial gamma-ray flashes, *J. Geophys. Res. Space Physics*, *118*, doi:10.1002/jgra.50188.

1. Introduction

1.1. TGF Theory Overview

[2] Terrestrial gamma-ray flashes (TGFs) are bright bursts of gamma rays, usually observed from space, that originate from the Earth's atmosphere [*Fishman et al.*, 1994; *Smith et al.*, 2005; *Briggs et al.*, 2010; *Marisaldi et al.*, 2010]. Although they were originally hypothesized to be produced at sprite altitudes, it is now generally accepted that they are produced at thundercloud altitudes, below about 20 km [*Cummer et al.*, 2005; *Dwyer and Smith*, 2005; *Carlson et al.*, 2007]. The gamma rays are thought to be produced by relativistic runaway electron avalanches (RREAs), accelerated by electric fields inside thunderclouds [*Wilson*, 1925; *Gurevich et al.*, 1992; *Lehtinen et al.*, 1999], but there is as yet no consensus on the mechanism(s) for generating the large number of runaway electrons required to account for the observed luminosities of TGFs. The two TGF models that have emerged in recent years are (1) the relativistic feedback discharge model for which RREA are generated by a self-sustaining discharge initiated by a single seed particle and involving backward propagating positrons and backscattered X-rays [*Dwyer*, 2003, 2005, 2007, 2008, 2012] and (2) lightning leader models for which RREAs are seeded by a large number of runaway electrons produced in the very high fields associated with the lightning leaders [*Gurevich*, 1961; *Dwyer*, 2004, 2008; *Dwyer et al.*, 2005, 2010; *Moss et al.*, 2006; *Gurevich et al.*, 2007; *Carlson et al.*, 2009, 2010; *Celestin and Pasko*, 2011, 2012; *Celestin et al.*, 2012; *Xu et al.*, 2012].

[3] *Dwyer* [2012] presented computer simulations of the relativistic feedback discharge model showing consistency with the fluences, time-intensity profiles, and pulse structures observe in TGFs. Furthermore, relativistic feedback limits the electric fields and hence the avalanche multiplication factors in air [*Dwyer*, 2003], affecting the alternate models [*Dwyer*, 2008]. As a result, even if the relativistic feedback is not directly involved in the production of the runaway electrons in a TGF, it still should be considered when modeling the electric fields and runaway electron production used in other TGF models. For example, *Dwyer* [2008] showed that when the limits on the avalanche multiplication imposed by relativistic feedback are included, RREAs seeded by atmospheric cosmic rays produce too few runaway electrons to be a viable explanation of TGFs.

[4] It has also been shown that the runaway electron luminosities of energetic radiation inferred from lightning near the ground could account for TGF originating from thunderclouds [*Dwyer*, 2008; *Saleh et al.*, 2009; *Dwyer et al.*, 2010]. These TGF models are based upon the observations of X-ray emissions from stepped leaders from natural and cloud-to-ground lightning [*Moore et al.*, 2001; *Dwyer et al.*, 2005] and from dart, dart-stepped, and chaotic leaders from rocket-triggered lightning [*Dwyer et al.*, 2003; *Dwyer et al.*, 2004, 2010; *Howard et al.*, 2008, 2010; *Hill et al.*, 2012; *Saleh et al.*, 2009; *Schaal et al.*, 2012]. It has been suggested that these X-rays are produced by so-called cold runaway electron production, more accurately "high field runaway" [*Dwyer*, 2008], in the high field regions generated by the leaders [*Gurevich*, 1961; *Dwyer*, 2004; *Moss et al.*, 2006]. For most lightning measured near the ground, the runaway electrons gain only a few hundred keV up to a few MeV of kinetic energy in the high field region of the

[1]Department of Physics and Space Sciences, Florida Institute of Technology, Melbourne, Florida, USA.
[2]Electrical and Computer Engineering Department, Duke University, Durham, North Carolina, USA.

Corresponding author: J. Dwyer, Department of Physics and Space Sciences, Florida Tech, Melbourne, FL 32901, USA. (jdwyer@fit.edu)

©2013. American Geophysical Union. All Rights Reserved.
2169-9380/13/10.1002/jgra.50188

lightning ($E > E_{th}$), resulting in very little RREA multiplication [*Dwyer et al*., 2004; *Dwyer*, 2004], since one RRE avalanche length requires an energy gain of about 7 MeV. As a result, the energy spectra of the X-ray emissions from lightning are much softer than the energy spectra of TGFs. On the other hand, for lightning inside thunderclouds, it has been speculated that the runaway electrons generated by lightning could continue to run away in the large-scale electric field of the thundercloud, experiencing RREA multiplication [e.g., *Dwyer*, 2008]. Alternatively, it has been suggested that the electric field produced by the lightning channel itself might be large enough for lightning inside thunderclouds to generate RREA multiplication [e.g., *Carlson et al*., 2009, 2010; *Celestin and Pasko*, 2011, 2012; *Celestin et al*., 2012]. In either case, these lightning models suppose that there is a pulse of seed runaway electron, followed by some amount of RREA development.

[5] In this paper, we shall parametrically model the injection of seed particles, from either feedback processes or high field/cold runaway to a high field region, and calculate the radio frequency (RF) emissions produced by the subsequent RREA propagation. These modeled RF emissions, which exhibit features that depend sensitively on the seed particle population, will then be compared with TGF-associated low frequency (LF) radio measurements [*Cummer et al*., 2011] in an effort to constrain the possible TGF source mechanisms.

1.2. Previous Radio Observations of TGFs

[6] One difficulty in distinguishing the various TGF models from satellite energetic photon measurements is that they all produce very similar gamma-ray energy spectra, angular distributions, and luminosities. Therefore, it is desirable to develop alternative methods of observing TGFs that can test the TGF models.

[7] In 2011, Cummer et al. analyzed the RF emissions during two Fermi/GBM TGFs [*Briggs et al*., 2010] and found that in both cases, there were distinct radio pulses that were simultaneous (to within an uncertainty of about 10 μs due to the uncertainty in the exact source location) with the TGFs and with inferred source currents that closely followed the observed gamma-ray time-intensity profiles. In other words, the inferred current pulses had similar shapes as the TGFs, and the peaks in the current pulses were simultaneous with the TGFs at the source. This indicated that the RF emissions were from currents closely associated with the gamma-ray production and suggested the possibility that they originated in the high energy electron acceleration process itself. *Dwyer* [2012] calculated the electrical currents generated during a TGF by the runaway electrons and drifting low-energy electrons and ions, ionized by the runaway electrons, and found that the length-integrated current moments from the TGF were many tens of kA km. This is comparable to the current moment in ordinary lightning and provided strong independent evidence that the radio pulses reported by *Cummer et al*. [2011] were in fact produced directly by the TGF itself.

[8] Observing RF emissions associated with TGFs has a long history with many groups reporting RF signatures near the time of the TGF [*Inan et al*., 1996, 2006; *Cummer et al*., 2005; *Stanley et al*., 2006; *Cohen et al*., 2006, 2010; *Lu et al*., 2010, 2011; *Shao et al*., 2010]. However, before the results of Cummer et al. and Dwyer, these RF signatures were always assumed to originate in accompanying lightning processes and not from the TGF itself. In particular, *Connaughton et al*. [2010] compared 50 Fermi/GBM TGFs with sferics measurements by WWLLN [*Jacobson et al*., 2006; *Rodger et al*., 2009] and found that 13 had WWLLN sferics that were emitted within 40 μs of the time of the TGF at the source. *Connaughton et al*. [2010] interpreted their results as showing a close association of IC lightning processes with the TGF. Based upon theoretical calculations and the work by *Cummer et al*. [2011], *Dwyer* [2012] suggested that rather than observing lightning, WWLLN was directly observing the VLF radiation from TGF, which naturally explains the close match in the times of the emission of the sferic and the gamma rays.

[9] In this work, we shall develop the theory of radio frequency emissions by terrestrial gamma-ray flashes. In particular, the radio emissions produced by the runaway electrons and resulting low-energy electrons and ions are calculated for the different TGF models discussed above. It is found that the radio frequency pulses produced by the TGF are large enough to measure and are also dependent on details of the source mechanism. Comparison of these calculations to measured TGF-associated signals provides experimental constraints on the mechanisms involved in TGF generation.

2. Overview of Radio Frequency Calculations

[10] We define an "avalanche pulse" as an avalanche of relativistic runaway electrons caused by a pulse of some number of injected energetic seed electrons. An avalanche pulse may be produced by a single seed electron caused by a backward propagating positron or a backscattered X-ray as described by the relativistic feedback model, or it could be produced by the rapid injection of a large number of seeds during a leader step, similar to that observed near the ground using X-rays. For the relativistic feedback model, the number of avalanche pulses, N_p, in a TGF is very large, e.g., $N_p \sim 10^{13}$. For the lightning leader model, in principle, there could be just one avalanche pulse in the TGF caused by the almost simultaneous injection of a very large number of seed particles. In that case, the TGF (at the source) might be very short, e.g., 30 ns long according to *Celestin et al*. [2012], *Celestin and Pasko* [2012], and *Xu et al*. [2012], and the larger duration seen in space is due to Compton scattering of the photons [*Celestin and Pasko*, 2012]. Alternatively, there might be many leader branches, each producing separate avalanche pulses in the TGF. *Celestin and Pasko* [2012] suggest that there may be on the order of 10 avalanche pulses in a TGF. Therefore, the number of avalanche pulses could range from 1 to about 10^{13}, depending upon the production mechanism involved.

[11] Whenever avalanches of runaway electrons are made, radio frequency emissions will also occur. Part of the emission comes from the acceleration and deceleration of the relativistic runaway electrons, but some comes from the drifting low-energy electrons and ions produced by the runaway electrons ionizing the air. Because the seeds of the runaway electron avalanches may be injected over time periods that are longer than the propagation times of the runaway electrons, the total duration of each avalanche pulse will be a combination of the seed electron injection time and

the time for the runaway electrons in the avalanche to propagate. A TGF is the superposition of some number of runaway electron avalanche pulses, and so the total radio emission from a TGF will be the superposition of the radio pulses produced by the individual avalanche pulses. The radiation field generated by an avalanche pulse is proportional to the time derivative of the resulting electrical current moment. As a result, for a given number of runaway electrons, shorter avalanche pulses will produce larger RF amplitudes than longer ones. Furthermore, shorter avalanche pulses generate more spectral energy density at higher frequencies than do longer ones. If the total number of avalanche pulses is very large, then the current moments from the individual avalanche pulses will add together to give a smooth current moment profile that roughly follows the overall profile of the gamma-ray luminosity at the source. However, if the TGF is composed of just a few avalanche pulses produced by the injection of many seed particles in very short windows of time, as has been discussed by some authors [e.g., *Carlson et al.*, 2009, 2010; *Celestin and Pasko*, 2011, 2012; *Celestin et al.*, 2012], then the TGF may appear as a series of very large RF pulses, resulting in RF signals that are distinct from TGFs composed of large numbers of avalanches.

[12] In order to investigate the RF emissions from TGFs, emission processes shall be modeled by separately calculating the contributions to the electrical currents produced during a TGF by individual avalanche pulses. This is outlined in the diagram shown in Figure 1. A list of symbols used in the text is given in Table 1.

3. Seed Electrons

3.1. Arbitrary Source Function

[13] As discussed above, the runaway electron avalanches are potentially seeded by individual particles such as positrons, X-rays, or cosmic rays, or the runaway electron emissions from lightning leaders, either from the leader tip or by streamers surrounding the leader.

[14] Generally, we shall write the source function describing the injection of seed runaway electrons in the jth avalanche pulse as $s_j^{\text{seed}}(t)$, i.e., the number of seed particles injected per second. The electrical current density (A/m^2) generated by the resulting runaway electron avalanche pulse (low-energy electrons will be considered below) is then the convolution

$$\vec{J}_j^{re}(x,y,z,t) = s_j^{\text{seed}} \circ \vec{J}_{re} = \int_{-\infty}^{\infty} s_j^{\text{seed}}\left(t'\right) \ \vec{J}_{re}\left(x,y,z,t-t'\right) dt', \tag{1}$$

where $\vec{J}_{re}$ is the electrical current density produced by the runaway electrons seeded by one particle and $f \circ g \equiv \int_{-\infty}^{\infty} f\left(t'\right) \ g\left(t-t'\right) \mathrm{d}t'$ is the convolution of the functions f and g over time.

3.2. Simple Model of Source Function

[15] For the lightning leader models, it is currently not well understood how lightning leaders emit runaway electrons, so it is not possible to quantitatively predict the pulse shape or the duration of the seed runaway electrons by extrapolating ground observations to thundercloud altitudes.

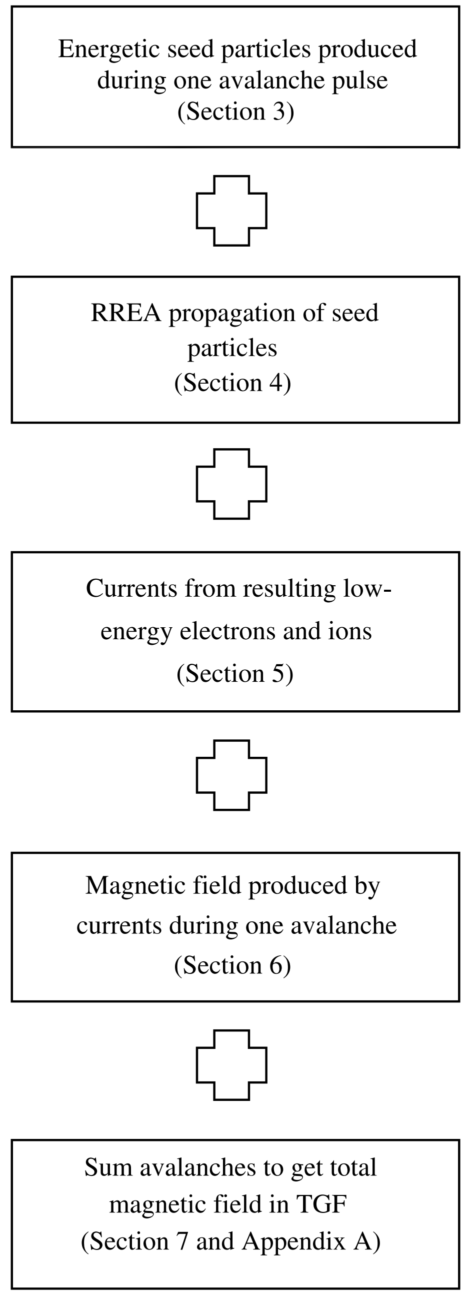

Figure 1. Diagram of how the RF emissions from a TGF are calculated in this paper.

Consequently, we shall assume that the shape of the seed runaway electron pulse is Gaussian. We shall leave the duration of the seed electron pulse as a free parameter, which we assume may range from 30 ns up to 1 μs (section 9). Although there is little justification for this specific pulse shape, it has the advantage of not producing high-frequency Fourier components due to artificial sharp edges, such as would result from a box function. Also, in this analysis, we shall consider the sum of many such pulses, so the exact shape should not matter. Furthermore, the Gaussian is a simple function that may be considered to represent the average waveform. Consequently, we shall write the source function (electrons/second) describing the injection of seed runaway electrons in the jth avalanche pulse at time t_j as

Table 1. List of Symbols, in the Approximate Order That They Appear in the Text. In Addition, the Fourier Transform of a Function, f, Is Denoted by the Notation $\widetilde{f}$.

Symbol	Units	Meaning
n	Unitless	Density of air relative to that at sea level at standard conditions (1 atm and 0°C)
x, y, z	m	Position (z is in the vertical direction)
t	s	Time
$e = 1.6 \times 10^{-19}$ C	C	Charge of electron
N_p	Unitless	Number of avalanche pulses
$\vec{J}_{re}$	A/m^2	Electric current density produced by the runaway electrons seeded by one particle
$\vec{J}_j^{re}$	A/m^2	Electric current density produced by the runaway electrons in the jth avalanche pulse
s_j^{seed}	s^{-1}	Number of seed particles injected in the jth pulse
N_j^{seed}	Unitless	Number of energetic seed electrons injected during the jth avalanche pulse
σ_s	s	RMS duration of the seed particle pulse
N_{re}	Unitless	Number of runaway electrons in a RREA
λ	m	RREA avalanche length
E	V/m	Electric field
$E_d = 2.76 \times 10^5$V/m $\times\, n$	V/m	Electric field parameter used to calculate λ
$E_{th} = 2.84 \times 10^5$V/m $\times\, n$	V/m	RREA threshold field
N_o	Unitless	Number of energetic seed electrons for a RREA
Γ	V/m^2	Rate of change of the electric field with height at the end of the avalanche region (where $E = E_{th}$)
κ	m	Vertical thickness of RREA
v	m/s	Speed of runaway electron avalanche
ξ	Unitless	Number of runaway electron avalanche lengths
N_j^{re}	Unitless	Maximum number of runaway electrons produced during the jth avalanche pulse
$\vec{J}_j^{le}$	A/m^2	Electric current density due to the drifting low-energy electrons in the jth avalanche pulse
G_{le}	s^{-1}	Green's function for low-energy electron current
μ_e	m^2/V s	Mobility of low-energy electrons
α	m^{-1}	The number of electron-ion pairs created per unit length per runaway electron
τ	s	Low-energy electron attachment time
$\vec{J}_j^{\mathrm{ions}}$	A/m^2	Electric current density due to the drifting ions in the jth avalanche pulse
G_{ions}	s^{-1}	Green's function for ion current
$\mu_+ = (1.4 \times 10^{-4}$ m^2/V s$)/n$	m^2/V s	Mobility of positive ions in air
$\mu_- = (2.1 \times 10^{-4}$ m^2/V s$)/n$	m^2/V s	Mobility of negative ions in air
τ_{ion}	s	Lifetime of the drifting ions
$\vec{J}_j$	A/m^2	Total electric current density in the jth avalanche pulse
$\vec{B}_j$	Tesla	Magnetic field from the jth avalanche pulse
$\vec{R}_o$	m	Position vector of observer
$\vec{R}$	m	Displacement vector from the current source to the observer
c $= 3.0 \times 10^8$ m/s	m/s	Speed of light
$\varepsilon_o = 8.85 \times 10^{-12}$ C^2/J m	C^2/J m	Permittivity of free space
$\vec{B}_{re}$	Tesla	Magnetic field produced by the runaway electrons in an avalanche seeded by one particle
i	Unitless	Imaginary number
$\hat{\phi}$	Unitless	Azimuthal unit vector
ω	radians/s	Angular frequency
θ	radians	Polar angle
β	Unitless	Speed of runaway electron avalanche divided by c
N^{TGF}	Unitless	Total number of runaway electrons in a TGF
a_j	Unitless	Fraction of runaway electrons in a TGF in the jth avalanche pulse
f_{TGF}	s^{-1}	Normalized time-intensity profile of TGF
r	s^{-1}	Rate of avalanche pulses
t_j	s	Time of the jth avalanche pulse
$\vec{S}$	W/m^2	Poynting vector
$\vec{B}_{\mathrm{rad}}$	Tesla	Radiation part of the magnetic field
F_{rad}	J/m^2	Energy per unit area from electromagnetic radiation (also per unit angular frequency)
σ_{TGF}	s	RMS duration of TGF (at source)
$\zeta_\pm$	s^{-1}	Parameter used to describe shape of runaway electron time-intensity function
Ω	m	Total path length of all runaway electrons in a TGF
T_{50}	s	Duration of a TGF (time difference between the first 25% and the first 75% of the counts)
$\vec{E}_{\mathrm{rad}}$	V/m	Radiation part of the electric field
$\vec{I}_{re}$	A m	Current moment of runaway electrons
$\vec{I}_j$	A m	Current moment in jth avalanche pulse
$\vec{I}_{\mathrm{total}}$	A m	Total current moment of TGF

$$s_j^{\text{seed}}(t) = \frac{N_j^{\text{seed}}}{\sqrt{2\pi\sigma_s^2}} \exp\left(\frac{-(t-t_j)^2}{2\sigma_s^2}\right), \tag{2}$$

where N_j^{seed} is the number of energetic seed electrons injected during the jth avalanche pulse and σ_s gives the duration of the seed particle pulse. In this work, for simplicity, we shall assume that all pulses of seed electrons have the same duration, but we will allow the number of seeds electrons per pulse to vary. If, in the future, a different function is found to better describe the injection of seed particles, then the change may be implemented by following the same procedure outlined in this work.

[16] Alternatively, for the relativistic feedback model, each avalanche pulse is seeded by approximately one seed electron. In this case, equation (2) becomes a Dirac delta function with $N_j^{\text{seed}} = 1$, and equation (2) is just $\overrightarrow{J_j^{re}} = \overrightarrow{J}_{re}$.

4. Relativistic Runaway Electron Avalanches (RREAs)

4.1. Arbitrary RREA Propagation

[17] Let us next consider the relativistic runaway electron propagation. The number of runaway electrons in a RREA, N_{re}, is described by

$$dN_{re} = N_{re}\frac{dz}{\lambda}, \tag{3}$$

where the e-folding length, λ, describes the avalanche length when $\lambda > 0$ and the attenuation length when $\lambda < 0$. The avalanche and attenuation length are both approximately described by empirical expression

$$\lambda = \frac{7.3 \times 10^6 V}{(E - E_d)}, \tag{4}$$

determined from fits to Monte Carlo simulation results [*Dwyer*, 2003; *Coleman and Dwyer*, 2006; *Dwyer*, 2012], where λ has units of meters and E has units of V/m. The parameter $E_d = 2.76 \times 10^5$V/m $\times\, n$ is found from Monte Carlo simulations to be approximately equal to the runaway avalanche threshold field $E_{th} = 2.84 \times 10^5$V/m $\times\, n$ when $E > E_{th}$ and $E_d \approx 3.2 \times 10^5$V/m $\times\, n$ when $E < E_{th}$, with n being the density of air at that altitude relative to that at sea level at standard conditions. For this work, for simplicity, $E_d = E_{th}$ will be used for all values of the electric field.

[18] Let us consider an electric field such that $E > E_{th}$ between $z_o < z < 0$, with $\overrightarrow{E}(z) = -E(z)\hat{z}$. In other words, the coordinate system is chosen so that the avalanches move in the +z direction and the end of the avalanche region is at $z = 0$. For TGFs generated inside thunderclouds, the origin of this coordinate system might correspond to an altitude of roughly 10–20 km. For an avalanche starting at position z_o and measured at position z, equation (3) can be integrated directly to give

$$N_{re}(z, z_o) = N_o \exp\left(\int_{z_o}^{z} \frac{dz}{\lambda}\right), \tag{5}$$

where N_o is the number of energetic seed electrons injected at position z_o, at the start of the avalanche region.

4.2. Simple Model of RREA Propagation

[19] Because $z = 0$ is chosen to be the end of the avalanche region, $E > E_{th}$ for $z_o < z < 0$ and $E < E_{th}$ otherwise. Furthermore, most of the runaway electrons and the resulting electrical current will be located near $z = 0$, where the avalanche is at its peak. As a result, keeping just the first two terms in the Taylor expansion of the field about z, we may approximate the electric field as $E = E_{th} - \Gamma z$, where $\Gamma = \left|\frac{dE}{dz}\right|$ is evaluated at $z = 0$. Substituting this electric field into equation (4) and then doing the integration in equation (5) gives $N_{re}(z) = N_{\max} \exp\left(\frac{-z^2}{2\kappa^2}\right)$, where $\kappa = \left(\frac{7.3\times10^6 V}{\Gamma}\right)^{1/2}$ and $N_{\max} = N_o \exp\left(\frac{z_o^2}{2\kappa^2}\right) = N_o \exp(\xi)$ is the number of runaway electrons at $z = 0$. In other words, the number of runaway electrons near the end of the avalanche region, where the avalanche is largest, is approximately a Gaussian function of position.

[20] For such a runaway electron avalanche located at $x = y = z = 0$ at time $t = 0$, the electrical current density (generated by just the runaway electrons, i.e., $N_o = 1$) per seed runaway electron at $z = 0$ is given by [*Dwyer et al.*, 2009]

$$\overrightarrow{J}_{re}(x, y, z, t) = -ev\exp(\xi)\exp\left(\frac{-z^2}{2\kappa^2}\right)\delta(v\ t - z)\delta(x)\delta(y)\hat{z}, \tag{6}$$

where $v = 0.89c$ is the speed of the runaway electron avalanche [*Coleman and Dwyer*, 2006], e is the charge of the electron, and δ is the Dirac delta function, which has units of m^{-1} in this case. Note that the diffusion in the lateral (x and y) and longitudinal (z) directions is not included in equation (6). However, the effects of diffusion, which increases the apparent duration of the current pulse seen by an observer, may be approximately taken into account by increasing the duration of the seed electrons in equation (1).

[21] When equation (6) is plugged into equation (1), the resulting product $N_j^{re} = N_j^{\text{seed}} \exp(\xi)$ is the maximum number of runaway electrons at the end of the avalanche region produced during the jth avalanche pulse. This number could change from avalanche to avalanche because the number of seed electrons changes and/or the avalanche multiplication factor changes. We allow both possibilities by allowing the product N_j^{re} to vary as a function of j.

[22] Clearly, other choices could be made for $N_{re}(z)$, depending upon the details of the electric field considered. We view equation (6) as a reasonable approximation for describing the runaway electron avalanche propagation that allows us make calculations without knowing the details of such electric fields. However, other choices may be implemented following the methods described in this work.

5. Low-Energy Electrons and Ions

5.1. Low-Energy Electrons

[23] As the runaway electrons propagate, they ionize the air creating free low-energy (few eV) electrons and light ions, which drift in the electric field producing additional currents. In fact, the currents from the low-energy electrons and ions are much larger than that from the runaway electrons directly. The low-energy electrons rather quickly attach to oxygen on a timescale, τ, due to two- and three-body attachment processes, creating negative ions. At TGF

altitudes, τ is on the order of 1 μs. The electrical current density (A/m^2) due to the drifting low-energy electrons for each avalanche pulse is

$$\overrightarrow{J_j^{le}}(x,y,z,t) = \overrightarrow{J_j^{re}} \circ G_{le} = \int_{-\infty}^{\infty} \overrightarrow{J_{\mathrm{j}}^{re}}\left(x,y,z,t'\right)\ G_{le}\left(t-t'\right)\mathrm{d}t', \quad (7)$$

where

$$G_{le}\left(t-t'\right) = \mu_e E\alpha \exp\left(-\left(t-t'\right)/\tau\right) S\left(t-t'\right), \quad (8)$$

and $S(t-t')$ is the step function. The Green's function G_{le} is the particle current of low-energy electrons (electrons/second) produced by each runaway electron [see *Dwyer et al.*, 2009]. In equation (8), μ_e is the low-energy electron mobility (in V m^2/s), E is the magnitude of the electric field (in V/m), and α is the number of electron-ion pairs created per unit length per runaway electron (in m^{-1}). τ is the attachment time of the low-energy electrons to air (in seconds), principally via two- and three-body attachment processes [*Morrow and Lowke*, 1997; *Liu and Pasko*, 2004]. Note that rate of electron losses due to electron-ion recombination is much smaller than the attachment rate for the cases under consideration here and so will be ignored in this paper.

5.2. Ion Drift

[24] Similarly, the current density (Amps/m^2) from the ions for each avalanche pulse is

$$\overrightarrow{J_j^{\mathrm{ions}}}(x,y,z,t) = \overrightarrow{J_j^{re}} \circ G_{\mathrm{ions}} = \int_{-\infty}^{\infty} \overrightarrow{J_j^{re}}\left(x,y,z,t'\right)\ G_{\mathrm{ions}}\left(t-t'\right)dt', \quad (9)$$

where the Green's function

$$G_{\mathrm{ions}}\left(t-t'\right) = \left\{\mu_+ E\alpha\ \exp\left(-\left(t-t'\right)/\tau_{\mathrm{ion}}\right) + \frac{\mu_- E\alpha\ \left(\exp\left(-\left(t-t'\right)/\tau_{\mathrm{ion}}\right) - \exp\left(-\left(t-t'\right)/\tau\right)\right)}{\left(1-\tau/\tau_{\mathrm{ion}}\right)}\right\} S\left(t-t'\right). \quad (10)$$

In equation (10), μ_+ and μ_- are the magnitudes of the mobilities of the positive and negative ions, respectively, and τ_{ion} is the lifetime of the drifting ions, which includes effects of ion-ion and ion-electron recombination and attachment of ions to cloud particles. Because the recombination processes are nonlinear, equation (10) is an approximation. τ_{ion} is also used to qualitatively include the effect of the exponentially decreasing current from the ions due to the discharging of the electric field. However, for the cases under investigation in this paper, the drift of the ions will be of secondary importance, and so we opt for the simplicity over accuracy here.

5.3. Total Current

[25] The total current density generated from all sources during the jth avalanche pulse is then

$$\overrightarrow{J_j}(x,y,z,t) = \overrightarrow{J_j^{re}}(x,y,z,t) + \overrightarrow{J_j^{le}}(x,y,z,t) + \overrightarrow{J_j^{\mathrm{ions}}}(x,y,z,t). \quad (11)$$

In equations (8) and (10), the electric field magnitude may be a function of position. However, since the number of runaway electrons peaks at the end of the avalanche region and most of the current is generated there, where $E = E_{th}$, we shall assume that $E = E_{th}$ in equations (8) and (10). This approximation is reasonable since the field is assumed to decrease linearly at the end of the avalanche region, and so E_{th} is the average field in that region. We shall also approximate μ_e, μ_+, μ_-, α, and τ as being fixed and equal to the values found at the altitude at the end of the avalanche region. This is well justified, since the length scale, κ, is expected to be on the order of hundreds of meters (e.g., 50–220 m is used in this work), much smaller than the scale height of the atmosphere.

6. Electromagnetic Fields Produced by an Avalanche Pulse

[26] Once the electrical current is known, the magnetic field (in Tesla), for the jth avalanche pulse, observed at position $\overrightarrow{R_o}$ and time t is given by Jefimenko's equation [*Griffiths*, 1999; *Uman*, 2001]:

$$\begin{aligned}\overrightarrow{B_j}\left(\overrightarrow{R_o},t\right) &= \frac{1}{4\pi\varepsilon_o c^2}\int d^3\overrightarrow{x'}\int dt'\,\frac{\left(\overrightarrow{J_j}(x',y',z',t')\times\hat{R}\right)\delta(t'-t+R/c)\,S(t-t')}{R^2}\\ &+\frac{1}{4\pi\varepsilon_o c^2}\frac{\partial}{\partial t}\int d^3\overrightarrow{x'}\int dt'\,\frac{\left(\overrightarrow{J_j}(x',y',z',t')\times\hat{R}\right)\delta(t'-t+R/c)\,S(t-t')}{cR},\end{aligned} \quad (12)$$

where $\overrightarrow{R} = \overrightarrow{R_o} - \overrightarrow{x}'$. The first term in equation (12) is the so-called induction term, and the second term is the radiation term. With the current found above in equation (11), equation (12) could be calculated exactly using numerical methods. In order to gain physical insight, we will instead find analytical solutions by first calculating the Fourier transform of equation (12). To do this, we note that each term in equation (12) involves a convolution of the current with respect to time. Furthermore, each term in equation (11) also involves a convolution of the current in equation (6) with respect to time. Using the commutation property of convolutions, we may therefore rewrite equation (12) as

$$\overrightarrow{B_j} = \overrightarrow{B_{re}} \circ \mathrm{s}_{\mathrm{j}}^{\mathrm{seed}} + \left(\overrightarrow{B_{re}} \circ \mathrm{s}_{\mathrm{j}}^{\mathrm{seed}}\right) \circ \left(\mathrm{G}_{\mathrm{ions}} + \mathrm{G}_{le}\right), \quad (13)$$

In equation (13),

$$\overrightarrow{B}_{re}\left(\overrightarrow{R_o},t\right) = \frac{1}{4\pi\varepsilon_o c^2}\int d^3\overrightarrow{x}'\int dt' \frac{\left(\overrightarrow{J}_{re}\left(x',y',z',t'\right)\times\hat{R}\right)\delta\left(t'-t+R/c\right)\ S\left(t-t'\right)}{R^2} + \frac{1}{4\pi\varepsilon_o c^2}\frac{\partial}{\partial t}\int d^3\overrightarrow{x}'\int dt' \frac{\left(\overrightarrow{J}_{re}\left(x',y',z',t'\right)\times\hat{R}\right)\ \delta\left(t'-t+R/c\right)\ S(t-t')}{c\ R}, \tag{14}$$

with $\overrightarrow{J}_{re}$ given in equation (6). Since $\overrightarrow{J}_{re}$ is in the $-z$ direction, the cross product is in the $-\hat{\phi}$ direction.

[27] The Fourier transform of equation (13) is then

$$\tilde{\overrightarrow{B}}_j\left(\overrightarrow{R_o},\omega\right) = \sqrt{2\pi}\,\tilde{\overrightarrow{B}}_{re}\left(\overrightarrow{R_o},\omega\right)\ \tilde{s}_j^{\text{seed}}(\omega) + 2\pi\left(\tilde{\overrightarrow{B}}_{re}\left(\overrightarrow{R_o},\omega\right)\ \tilde{s}_j^{\text{seed}}(\omega)\right)\left(\tilde{G}_{\text{ions}}(\omega)+\tilde{G}_{le}(\omega)\right), \tag{15}$$

where the Fourier transform with respect to t is defined to be

$$\tilde{f}(\omega) \equiv \frac{1}{\sqrt{2\pi}}\int_{-\infty}^{\infty} f(t)\ \exp(i\omega t)dt. \tag{16}$$

[28] In equation (15), we use the property that the Fourier transform of $f\circ g$ is $\sqrt{2\pi}\tilde{f}\ \tilde{g}$. Note the Fourier transform of the magnetic field has units of Tesla seconds.

[29] Because the size of the emission region of the system, $\sim\kappa$, is assumed to be much smaller than the distance to the observer R, the radius R that appears inside the delta functions above may be expanded as $R \approx R_o - z'\cos\theta$, where R_o is the distance to the origin $z=x=y=0$ and θ is the polar angle with respect to the z axis. Note that it is not necessary to expand the radius in the denominators or the unit vector in the cross product, since the contributions from these higher-order terms is very small. It is necessary to keep the induction term, however, since it will make a significant contribution when many avalanche pulses are summed together. With these approximations,

$$\overrightarrow{B}_{re}\left(\overrightarrow{R_o},t\right) = \frac{-\hat{\varphi}\sin\theta}{4\pi\varepsilon_o c^2 R_o}\left(\frac{1}{R_o}+\frac{1}{c}\frac{\partial}{\partial t}\right)\int d^3\overrightarrow{x}'\int dt'\ J_{re}\left(x',y',z',t'\right)\ \delta\left(t'-t+R_o/c-\left(z'/c\right)\cos\theta\right)\ S\left(t-t'\right) \tag{17}$$

[30] Since $\overrightarrow{J}_{re}$ is in the $-z$ direction, the cross product is in the $-\hat{\phi}$ direction.

$$\overrightarrow{B}_{re}\left(\overrightarrow{R_o},t\right) = \frac{-\hat{\varphi}\ ev\ \sin\theta\ \exp(\xi)}{4\pi\varepsilon_o c^2 R_o(1-\beta\cos\theta)}\left(\frac{1}{R_o}-\frac{(t-R_o/c)v^2}{c\kappa^2(1-\beta\cos\theta)^2}\right)\exp\left(\frac{-(\mathrm{t}-\mathrm{R_o}/\mathrm{c})^2\mathrm{v}^2}{2\kappa^2(1-\beta\cos\theta)^2}\right) \tag{18}$$

[31] The Fourier transform of $\overrightarrow{B}_{re}\left(\overrightarrow{R_o},t\right)$ is

$$\tilde{\overrightarrow{B}}_{re}\left(\overrightarrow{R_o},\omega\right) = \frac{-\hat{\varphi}\ e\ \kappa\sin\theta\exp(\xi)}{4\pi\varepsilon_o c^2 R_o}\left(\frac{1}{R_o}-\frac{i\omega}{c}\right)\exp\left(\frac{-\omega^2\kappa^2(1-\beta\cos\theta)^2}{2\mathrm{v}^2}\right)\exp\left(\frac{i\omega\mathrm{R_o}}{\mathrm{c}}\right) \tag{19}$$

[32] The Fourier transform of s_j^{seed} is

$$\tilde{s}_j^{\text{seed}}(\omega) = \frac{N_j^{\text{seed}}}{\sqrt{2\pi}}\exp\left(\frac{-\omega^2\sigma_s^2}{2}\right)\exp\left(i\omega\ t_j\right). \tag{20}$$

[33] The Fourier transform of G_{le} is

$$\tilde{G}_{le}(\omega) = \frac{1}{\sqrt{2\pi}}\frac{\mu_e E\alpha}{\left(\frac{1}{\tau^2}+\omega^2\right)}\left(\frac{1}{\tau}+i\omega\right). \tag{21}$$

[34] The Fourier transform of G_{ion} is

$$\tilde{G}_{\text{ion}}(\omega) = \frac{\mu_+ E\alpha}{\sqrt{2\pi}}\frac{\left(\frac{1}{\tau_{\text{ion}}}+i\omega\right)}{\left(\frac{1}{\tau_{\text{ion}}^2}+\omega^2\right)} + \frac{\mu_- E\alpha}{\sqrt{2\pi}}\frac{1}{\left(1-\frac{\tau}{\tau_{\text{ion}}}\right)}\left[\frac{\left(\frac{1}{\tau_{\text{ion}}}+i\omega\right)}{\left(\frac{1}{\tau_{\text{ion}}^2}+\omega^2\right)}-\frac{\left(\frac{1}{\tau}+i\omega\right)}{\left(\frac{1}{\tau^2}+\omega^2\right)}\right]. \tag{22}$$

[35] Note that $\tilde{s}_j^{\text{seed}}$, $\tilde{G}_{le}$, and $\tilde{G}_{\text{ion}}$ are all unitless. Combining these results using equation (13) gives

$$\tilde{\overrightarrow{B}}_j\left(\overrightarrow{R_o},\omega\right) = \tilde{\overrightarrow{B}}^o\left(\overrightarrow{R_o},\omega\right)\ N_j^{re}\exp\left(i\omega t_j\right), \tag{23}$$

where $N_j^{re} = N_j^{\text{seed}}\exp(\xi)$ and

$$\tilde{\overrightarrow{B}}^o\left(\overrightarrow{R_o},\omega\right) = \frac{-\hat{\varphi}\ e\ \kappa\sin\theta}{4\pi\varepsilon_o c^2 R_o}\left(\frac{1}{R_o}-\frac{i\omega}{c}\right) \times\exp\left(\frac{-\omega^2\left[\sigma_s^2+\left(\kappa^2(1-\beta\cos\theta)^2/v^2\right)\right]}{2}\right)\exp\left(\frac{i\omega R_o}{c}\right) \times\left\{1+E\alpha\left(\mu_e-\mu_-\left(1-\frac{\tau}{\tau_{\text{ion}}}\right)^{-1}\right)\left(\frac{1}{\tau}-i\omega\right)^{-1} + E\alpha\left(\mu_+ +\mu_-\left(1-\frac{\tau}{\tau_{\text{ion}}}\right)^{-1}\right)\left(\frac{1}{\tau_{\text{ion}}}-i\omega\right)^{-1}\right\}. \tag{24}$$

7. Electromagnetic Field Produced by a Superposition of Avalanche Pulses

[36] The total magnetic field from all avalanche pulses making up a TGF is

$$\tilde{\overrightarrow{B}}_{\text{total}}\left(\overrightarrow{R_o},\omega\right) = \tilde{\overrightarrow{B}}^o\left(\overrightarrow{R_o},\omega\right)\sum_j N_j^{re}\exp\left(i\omega t_j\right) = \tilde{\overrightarrow{B}}^o\left(\overrightarrow{R_o},\omega\right)\ N_{\text{TGF}}\sum_j a_j\exp\left(i\omega t_j\right), \tag{25}$$

where $a_j = N_j^{re}/N_{\mathrm{TGF}}$ and N_{TGF} is the number of runaway electrons in the TGF. Then $\sum_j a_j = 1$. *Dwyer and Smith* [2005] used Monte Carlo simulations and the RHESSI TGF data to show that N^{TGF} is about 10^{17} if the source region is at a 15 km altitude.

[37] In reality, the a_j may vary from avalanche pulse to avalanche pulse and the rate of avalanche pulses may also change with time. However, in order to evaluate equation (25), we consider two simple cases: (1) each avalanche pulse produces the same number of runaway electrons, and the time of each avalanche pulse, t_j, follows the normalized probability distribution, $f_{\mathrm{TGF}}(t)$; and (2) the avalanche pulses occur at a constant rate, r, and the number of runaway electrons in the avalanche pulses follow the function, $f_{\mathrm{TGF}}(t)/r$. In both cases, f_{TGF} is a normalized function determined by the time-intensity profile of the TGF. The first scenario might describe a rapidly changing number of lightning branches, each producing the same number of runaway electrons. Or, it might describe the relativistic feedback mechanism, with the number of seeds generated by feedback changing with time. The second scenario might describe a fixed number of leader branches entering and then propagating through an avalanche region.

[38] For case 1, if there are a total of N_p avalanche pulses within a TGF, then the requirement that $\sum_{j=1}^{N_p} a_j = 1$ implies that $a_j = 1/N_p$. If there are a large number of avalanche pulses in the TGF, and we use the approximation $N_p \to \infty$, then $\frac{1}{N_p}\sum_{j=1}^{N_p} \exp(i\omega t_j) \to \sqrt{2\pi}\tilde{f}_{\mathrm{TGF}}(\omega)$, where $\tilde{f}_{\mathrm{TGF}}(\omega)$ is the Fourier transform of $f_{\mathrm{TGF}}(t)$.

[39] Similarly for case 2, if the rate of avalanche pulses is large and we use the approximation $r \to \infty$, then $\sum_j a_j \exp(i\omega t_j) \to r\int_{-\infty}^{\infty} \frac{f_{\mathrm{TGF}}(t)}{r}\exp(i\omega t)dt = \sqrt{2\pi}\tilde{f}_{\mathrm{TGF}}(\omega)$.

[40] Therefore, for either case, if the number of avalanche pulses in the TGF is large, then

$$\tilde{\vec{B}}_{\mathrm{total}}\left(\vec{R}_o,\omega\right) = \frac{-\hat{\varphi}\ e\ \kappa\ \sin\theta}{4\pi\varepsilon_o c^2 R_o}\left(\frac{1}{R_o} - \frac{i\omega}{c}\right) \times \exp\left(\frac{-\omega^2\left[\sigma_s^2 + \left(\kappa^2(1-\beta\cos\theta)^2/v^2\right)\right]}{2}\right) \times \exp\left(\frac{i\omega \mathrm{R_o}}{\mathrm{c}}\right)\mathrm{N_{TGF}}\sqrt{2\pi}\tilde{\mathrm{f}}_{\mathrm{TGF}}(\omega) \times\left\{1 + E\alpha\left(\mu_{\mathrm{e}} - \mu_-\left(1-\frac{\tau}{\tau_{\mathrm{ion}}}\right)^{-1}\right)\left(\frac{1}{\tau} - i\omega\right)^{-1} + E\alpha\left(\mu_+ + \mu_-\left(1-\frac{\tau}{\tau_{\mathrm{ion}}}\right)^{-1}\right)\left(\frac{1}{\tau_{\mathrm{ion}}} - i\omega\right)^{-1}\right\}. \quad (26)$$

7.1. Fluctuations

[41] When N_p or r is finite, fluctuations will remain after the avalanche pulses are summed, resulting in more energy at high frequencies compared with equation (26). To evaluate these fluctuations and the spectra energy density, it is useful to calculate the variance of the magnetic field over an ensemble of TGFs.

$$\left\langle\left|\tilde{B}_{\mathrm{total}}\right|^2\right\rangle = \left|\tilde{B}_o\right|^2 N_{\mathrm{TGF}}{}^2\left\langle\left|\sum_j a_j\exp(i\omega t_j)\right|^2\right\rangle, \quad (27)$$

where the $\langle\rangle$ symbol represents the average over an ensemble of similar TGFs. It is shown in section A that

$$\left\langle\left|\sum_j a_j\exp(i\omega t_j)\right|^2\right\rangle \approx 2\pi\ \tilde{f}_{\mathrm{TGF}}^2 + \frac{1}{N_p}. \quad (28)$$

[42] Combining equations (24), (27), and (28) gives

$$\left\langle\left|\tilde{B}_{\mathrm{total}}\right|^2\right\rangle = \left(\frac{e\ \kappa\ \sin\theta}{4\pi\varepsilon_o c^2 R_o}\right)^2\left[\frac{1}{R_o^2} + \frac{\omega^2}{c^2}\right]N_{\mathrm{TGF}}{}^2 \times\exp\left(-\omega^2\left[\sigma_s^2 + \left(\kappa^2(1-\beta\cos\theta)^2/v^2\right)\right]\right)\left(2\pi\ \tilde{f}_{\mathrm{TGF}}^2 + \frac{1}{N_p}\right) \times\left\{\left(1 + \frac{\left(\mu_e - \mu_-(1-\tau/\tau_{\mathrm{ion}})^{-1}\right)E\alpha}{\tau\left(\frac{1}{\tau^2}+\omega^2\right)} + \frac{\left(\mu_+ + \mu_-(1-\tau/\tau_{\mathrm{ion}})^{-1}\right)E\alpha}{\tau_{\mathrm{ion}}\left(\frac{1}{\tau_{\mathrm{ion}}^2}+\omega^2\right)}\right)^2 + \left(\frac{\left(\mu_e - \mu_-(1-\tau/\tau_{\mathrm{ion}})^{-1}\right)E\alpha\omega}{\left(\frac{1}{\tau^2}+\omega^2\right)} + \frac{\left(\mu_+ + \mu_-(1-\tau/\tau_{\mathrm{ion}})^{-1}\right)E\alpha\omega}{\left(\frac{1}{\tau_{\mathrm{ion}}^2}+\omega^2\right)}\right)^2\right\}. \quad (29)$$

In the square bracket, the $\frac{1}{R_o^2}$ part is the induction term and the $\frac{\omega^2}{c^2}$ part is the radiation term.

8. Spectral Energy Density

[43] If we drop the induction term in equation (29), then the Poynting vector (W/m^2) for the electromagnetic radiation is

$$\vec{S} = c^2 \varepsilon_o \vec{E} \times \vec{B} = c^3 \varepsilon_o B_{\rm rad}^2 \hat{R}_o, \tag{30}$$

where $\hat{R}_o$ is the unit vector in the radial direction and $B_{\rm rad}$ is the radiation part of the magnetic field. Parseval's theorem gives the spectral energy density (energy per unit frequency per unit area)

$$F_{\rm rad} = \int_{-\infty}^{\infty} \vec{S}\cdot\hat{R}_o dt = 2c^3 \varepsilon_o \int_0^{\infty} \left|\widetilde{B}_{\rm rad}\right|^2 d\omega, \tag{31}$$

where $\widetilde{B}_{\rm rad}$ is the radiation part of $\widetilde{B}_{\rm total}$.

[44] The factor of 2 out front comes from the negative frequencies. As a result, the spectral energy density of the TGF electromagnetic radiation becomes

$$\begin{aligned} F_{\rm rad}(\omega) = {} & 2c^3 \varepsilon_o |B_{\rm rad}|^2 = 2c^3 \varepsilon_o \left(\frac{e\,\kappa \sin\theta}{4\pi\varepsilon_o c^2 R_o}\right)^2 \left[\frac{\omega^2}{c^2}\right] N_{\rm TGF}{}^2 \\ & \times \exp\left(-\omega^2\left[\sigma_s^2 + \left(\kappa^2(1-\beta\cos\theta)^2/v^2\right)\right]\right)\left(2\pi \widetilde{f}_{\rm TGF}^2 + \frac{1}{N_p}\right) \\ & \times \left\{\left(1 + \frac{\left(\mu_e - \mu_-(1-\tau/\tau_{\rm ion})^{-1}\right)E\alpha}{\tau\left(\frac{1}{\tau^2}+\omega^2\right)} + \frac{\left(\mu_+ + \mu_-(1-\tau/\tau_{\rm ion})^{-1}\right)E\alpha}{\tau_{\rm ion}\left(\frac{1}{\tau_{\rm ion}^2}+\omega^2\right)}\right)^2\right. \\ & \left. + \left(\frac{\left(\mu_e - \mu_-(1-\tau/\tau_{\rm ion})^{-1}\right)E\alpha\omega}{\left(\frac{1}{\tau^2}+\omega^2\right)} + \frac{\left(\mu_+ + \mu_-(1-\tau/\tau_{\rm ion})^{-1}\right)E\alpha\omega}{\left(\frac{1}{\tau_{\rm ion}^2}+\omega^2\right)}\right)^2\right\} \end{aligned} \tag{32}$$

[45] Equation (32) is calculated as an ensemble average and is to be interpreted as the average spectral energy density for TGFs. We note that when RF measurements are made near the ground, the magnetic fields must be multiplied by another factor of 2 in order to take into account the image charges (currents) in the ground. Similarly, the spectral energy density should be multiplied by a factor of 4.

9. TGF Time Structure

[46] In order to evaluate equations (26) and (32), the overall time structure of the TGF, $f_{\rm TGF}(t)$, must be known in order to find $\widetilde{f}_{\rm TGF}(\omega)$. It is possible to get $f_{\rm TGF}(t)$ from spacecraft gamma-ray observations as long as care is taken to understand the effects of instrumental dead time and atmospheric propagation. *Briggs et al.* [2010] found that most TGFs observed by Fermi/GBM could be fit to either Gaussian or log-normal distributions. *Fishman et al.* [2011] noted that shorter TGFs appeared Gaussian, which may indicate that at least some of the time, the log-normal fits better due to the low-energy tail caused by Compton scattering in the atmosphere.

[47] To date, the only model that is sufficiently developed to explicitly calculate $f_{\rm TGF}(t)$ is the relativistic feedback discharge model [*Dwyer*, 2012]. *Dwyer* [2012] found that that in many cases, $f_{\rm TGF}(t)$ was approximately a symmetrical function that was often close to a Gaussian. Inspection of the various $f_{\rm TGF}(t)$ functions found by *Dwyer* [2012] shows that there are usually wings on both sides of the Gaussian function. This may be understood by the fact that according to the feedback model, the intensity of runaway electrons grows exponentially until the field discharges, reducing the feedback factor below one, the self-sustaining value. Once the number of runaway electrons is reduced, the free low-energy electrons quickly attach to air atoms and the conductivity drops, freezing in the feedback factor at a value below one. The intensity of runaway electrons then decreases exponentially with time. In summary, relativistic feedback predicts that $f_{\rm TGF}(t)$ will first grow as $\exp(t/\tau_i)$, where τ_i is the timescale for growth determined by the geometry of the high field region and the initial feedback factor. For later times, $f_{\rm TGF}(t)$ will decrease as $\exp(-t/\tau_f)$, where τ_f is the timescale for decay determined by the geometry of the high field region and the final feedback factor. At the peak of the TGF, simulations show that the transition between the exponentially growing and decaying functions is approximately Gaussian.

[48] It is found that all of the TGF pulses presented in *Dwyer* [2012] can be approximately fit to the simple function

$$f_{\rm TGF}(t) = f_0 \exp\left(\frac{-t^2}{2\sigma_{\rm TGF}^2}(1+\zeta_\pm|t|)^{-1}\right), \tag{33}$$

where $\zeta_\pm$ are positive numbers such that

$$\zeta_\pm = \begin{cases} \zeta_+ & t > 0 \\ \zeta_- & t \le 0 \end{cases},$$

and f_0 is chosen such that equation (33) is normalized. Equation (33) is approximately a Gaussian function when $|t| << 1/\zeta_\pm$. When $|t| >> 1/\zeta_\pm$, then equation (33) becomes either an exponentially growing or decaying function, as desired. In the limit that $\zeta_{\pm} \to 0$, equation (33) becomes a Gaussian. Furthermore, it is also found that equation (33) is a reasonably close approximation to a log-normal function as long as the log-normal function is not too asymmetrical, i.e., not too different from a Gaussian.

[49] For simplicity, let us first consider the Gaussian case

$$f_{\mathrm{TGF}}(t) = \frac{1}{\sqrt{2\pi\sigma_{\mathrm{TGF}}^2}} \exp\left(\frac{-t^2}{2\sigma_{\mathrm{TGF}}^2}\right), \tag{34}$$

where σ_{TGF} gives the duration of the TGF at the source. In this case, the Fourier transform of equation (33), which is used in equations (26), (28), (29), and (32), is

$$\widetilde{f}_{\mathrm{TGF}}(\omega) = \frac{1}{\sqrt{2\pi}} \exp\left(\frac{-\omega^2\sigma_{\mathrm{TGF}}^2}{2}\right). \tag{35}$$

[50] Equation (35) will be combined with equations (29) and (32) to give several key results of this paper. For a large number of avalanche pulses, N_p, the falloff in the spectral energy density at higher frequencies is mostly determined by σ_{TGF} in the exponential in equation (35). On the other hand, if the number of avalanche pulses is not large, because of the $1/N_p$ term in equations (29) and (32), the spectral energy density at higher frequencies may be orders of magnitude greater than if the number of avalanche pulses is very large. This offers a test of competing TGF models. By comparing the spectral energy density across the VLF and LF bands, the number of avalanche pulses that made up the TGF could in principle be measured or at least constrained.

[51] When equation (33) is used instead of a Gaussian function, the Fourier transform must be found numerically. Results using this function will be presented in section 12, when comparing the model with TGF-associated RF measurements.

10. Assumed TGF Parameters

[52] In this work, we shall present models corresponding to the average properties of TGFs and models that fit two specific TGFs presented in *Cummer et al*. [2011]. We first discuss the relationship between the parameters used in this paper and the spacecraft observations of TGF gamma rays.

10.1. TGF Intensities

[53] Note that equations (26), (29), and (32) all contain the combination $\kappa N_{\mathrm{TGF}} \widetilde{f}_{\mathrm{TGF}}$ or its square. This is the Fourier transform of the fluence of runaway electrons passing through the end of the avalanche region times the average (1σ) length over which the runaway electrons travel. To relate this quantity to real TGF observations, it is useful to introduce

$$\Omega = \int N_{\mathrm{TGF}}(z)\, dz, \tag{36}$$

the total runaway electron path length of the TGF, where $N_{\mathrm{TGF}}(z)$ is the number of runaway electrons as a function of height. Assuming that the source altitude is known from other means, then Ω is the parameter that is usually determined from spacecraft observations of the gamma rays, since the fluence of the Bremsstrahlung gamma rays at the source is proportional to the fluence of runaway electrons times the average distance that they travel. Indeed, the often quoted peak value, $N_{\mathrm{TGF}} = 10^{17}$, which was inferred from RHESSI observations [*Dwyer and Smith*, 2005], assumed that the electric field in the avalanche region was $E/n = 400$ kV/m and zero outside the avalanche region. Since this field abruptly (and perhaps unrealistically) decreases at the end of the avalanche region, the runaway electron profile, $N_{re}(z)$, is not Gaussian as is assumed above. Nevertheless, for this electric field, near the altitude of 15 km, $\Omega = 5.3 \times 10^{19}$ m, using $n = 0.17$ at 15 km [*Dwyer*, 2012]. A deeper source region would require a larger value for Ω. For example, for the same number of gamma rays exiting the top of a thundercloud, a 13 km source would require Ω to be about 4.1 times larger than a 15 km source [*Dwyer*, 2012]. Considering that the fluence of photons at the spacecraft may be generally underestimated due to instrumental dead times [*Grefenstette et al*., 2008] and choosing a 13 km source altitude to be consistent with recent lightning observations associated with TGFs [*Lu et al*., 2010; *Cummer et al*., 2011], for calculations in this paper, we shall use $\Omega = 2.2 \times 10^{20}$ m, unless otherwise specified. We note that *Dwyer* [2012] found that for the relativistic feedback discharge model, shorter TGFs often had larger numbers of runaway electrons. If this is correct, then shorter TGFs should be much easier to measure at radio frequencies, both because of the larger N_{TGF} and the dependence on the duration that appears in equations (26), (29), and (32) above. For the Gaussian profile introduced in section 4, equation (35) gives $\Omega = \sqrt{2\pi}\kappa N_{\mathrm{TGF}}$. Therefore, we shall use $\kappa N_{\mathrm{TGF}} = 8.8 \times 10^{19}$, unless otherwise specified.

10.2. TGF Durations

[54] When inferring the TGF duration and time-intensity profile, the effects of Compton scattering in the atmosphere and instrumental dead time are important. Compton scattering will produce a substantial tail that may be as long or longer than the TGF source duration, especially at low energies. Furthermore, the Fermi TGF events are often presented as the sum of 12 NaI detectors and two BGO detectors. Because the NaIs are only sensitive to energies from 8 keV to about 1 MeV, and the BGOs are sensitive to energies above ~100 keV, the effect is to over emphasize the Compton tail and hence the duration of the TGFs [*Fishman et al*., 2011]. A better method of determining the TGF source duration, without doing addition modeling of the atmospheric propagation, is to only include data above 300 keV, where Compton scattering is reduced. *Fishman et al*. [2011] studied the widths of TGFs and reported the T_{50} widths to range from ~50 μs up to about ~700 μs, with 100 μs being the median T_{50} pulse duration. T_{50} is defined to be the time difference between the first 25% of the gamma-ray counts and the first 75% of the gamma-ray counts. Assuming a Gaussian distribution as in equation (33) gives $\sigma_{\mathrm{TGF}} = 0.75\ T_{50}$. Therefore, according to Fishman et al., σ_{TGF} ranges from about 38 μs up to about 0.5 μs, with these durations likely overestimating to some extent the true durations. Additional cases of Fermi TGFs have been published in which σ_{TGF} is about 15 μs [*Cummer et al*., 2011], which we shall also model in section 12.

10.3. Avalanche Pulse Properties

[55] For most of the calculations presented in this work, we shall assume that $\kappa = 50$ m/n, where n is the density of air with respect to the sea level value, which is comparable to the value used by *Dwyer and Smith* [2005]. At 13 km, with $n = 0.23$, this gives $\kappa = 220$ m. The requirement that $\kappa\ N_{\mathrm{TGF}} = 8.8 \times 10^{19}$ then implies that $N_{\mathrm{TGF}} = 4.0 \times 10^{17}$. The Celestin, Xu, and Pasko TGF model invokes a very short travel distance for the runaway electrons. The 1/e stopping distance of the (7 MeV average energy) runaway electrons is about 27 m/n, which is 120 m at 13 km. Assuming that the runaway electrons are produced in a very short distance and then quickly lose energy and stop, we find the minimum value of κ at 13 km is about 50 m, which we shall use for this model.

[56] The source duration σ_s is model dependent and is not known *a priori*. For lightning measured near the ground, the X-ray pulses are observed to be associated with the leader step formation process in stepped and dart-stepped leaders [*Dwyer et al.*, 2005; *Howard et al.*, 2008], and the X-rays are usually observed to be emitted in a time less than 1 microsecond (e.g., ~0.2 μs), implying that the source of seed runaway electrons also has a duration of less than 1 μs during each leader step. It is not known how the duration of these pulses scales with air density, but assuming a 1/n scaling law, this gives $\sigma_s \sim 1$ μs at TGF source altitudes. On the other hand, *Celestin et al.* [2012] modeled the runaway electron production from lightning leaders inside thunderclouds in order to explain the AGILE TGF observation of a high energy power-law tail extending up to 100 MeV [*Tavani et al.*, 2011]. In their model, they assume that the runaway electron emission by the lightning lasts less than 30 ns. They extended this model to explain all TGFs by assuming that multiple branches, each emitting a short runaway electrons avalanche, combine to make a TGF [*Xu et al.*, 2012]. We shall use $\sigma_s \sim 30$ ns for the Celestin, Xu, and Pasko model and $\sigma_s \sim 1$ μs for runaway electron emissions from stepped leaders similar to that observed near the ground. Because we lack a detailed understanding of how runaway electrons might be produced by lightning, for simplicity, we shall generalize these two scenarios and refer to the source time of $\sigma_s \sim 30$ ns as a "fast lightning source," and we shall refer to the source time of $\sigma_s \sim 1$ μs as a "slow lightning source." As will be seen below, shorter source durations increase the spectral energy density at the higher frequencies and longer durations reduce it.

[57] Similarly, the number of avalanche pulses, N_p, which is equal to the number of seed runaway electron pulses is not known *a priori*. Although, in principle, N_p could be as small as 1, such narrow TGFs have not been observed. *Celestin and Pasko* [2012] argue that the avalanches have an average spacing of about 10 μs. For $\sigma_{\mathrm{TGF}} = 75$ μs, this implies that there are about 30 pulses. An argument by *Carlson et al.* [2010] and *Celestin and Pasko* [2011] why TGFs are emitted by lightning inside thunderclouds and not near the ground is that the lightning leaders near the ground are heavily branched and so share the available charge causing the electric field to be too small on each branch to generate RREA and produce a TGF. Following this reasoning, if this model is correct, we would not expect N_p to be much larger than 30 if lightning leader tip are the source of the runaway electrons. On the other hand, if streamers are impulsively emitting runaway electrons as they propagate through the high field region of the thundercloud, then N_p could in principle be very large. As a result, we shall leave N_p as a free parameter and will present results for N_p ranging from 30 up to 10^4 for the two lightning source durations. Note that N_p cannot equal 1 for either the fast or slow lightning sources, since even with Compton scattering in the atmosphere, the duration of the TGF would be much too short to be consistent with spacecraft observations.

[58] On the other hand, it is possible that the TGF is not produced by runaway electrons generated by lightning leaders or streamers and instead are produced by a large number of backwards propagating positrons or backscattered X-rays as described by the relativistic feedback model [*Dwyer*, 2012]. This is equivalent to a very large number of distinct source pulses composed of individual particles, as discussed in section 3.2. The models considered in the paper are summarized in Table 2.

10.4. Other Parameters

[59] For real TGFs, the electric field in the current producing region may vary both in space and time. As a result, the constant field used in equations (8) and (10) to calculate the currents from the drifting low-energy electrons and ions is an approximation. To improve on this, a detailed, self-consistent model of the TGF and the electric field is required. To date, this is only possible for the relativistic feedback discharge model [*Dwyer*, 2012]. Rather than just calculating the RF emissions for this specific model, we approximate the field as a constant, so that it may be applied to all models. One common feature of all TGF models is that the runaway electron fluxes, and hence the electrical currents densities, are largest at the end of the avalanche region where $E = E_{th} = 284$ kV/m $\times\ n$. As discussed in section 4, E_{th} is also approximately the average field near in this region. Therefore, in this paper, we shall use set $E = E_{th}$, calculated at the altitude of the TGF.

[60] The discharging of the electric field may also affect the electrical currents of the drifting ions [*Dwyer* 2008], reducing this current approximately exponentially over time. Although this decrease is not explicitly modeled in this work, again because it would require a detailed, self-consistent model of the TGF and the electric field, we may roughly include this decrease in the ion loss time, τ_{ion}. We somewhat arbitrarily set $\tau_{\mathrm{ion}} = 10^{-3}$ s will be used in this work, which is consistent with the ion current relaxation times found from detailed simulations by *Dwyer* [2012].

[61] In section 11, unless otherwise stated, we shall present results at a radial distance of $R_o = 500$ km, which is about the same distance from the TGF to the sensors used by *Cummer et al.* [2011], and $\theta = \pi/2$ (broadside). At this distance, the field is dominated by the radiation term for most of the frequencies of interest.

Table 2. TGF Model Parameters

Model	Name of Model	N_p	σ_s (μ s)	κ (m)
A	Fast lightning source (Celestin, Xu, and Pasko)	30	0.03	50
B	Slow lightning source 1	100	1	220
C	Slow lightning source 2	10000	1	220
D	Relativistic feedback discharge	10^{13}	0	220
E	Infinite number of avalanche pulses	∞	0	220

[62] The mobilities of the ions are $\mu_+ = (1.4 \times 10^{-4}\,\mathrm{m^2/V\,s})/n$, $\mu_- = (2.1 \times 10^{-4}\,\mathrm{m^2/V\,s})/n$ [*Cobine*, 1941]. Unlike the ions, the electron's mobility, μ_e, is sensitive to the electric field magnitude. The mobility is found using data from *Morrow and Lowke* [1997] and *Liu and Pasko* [2004]. The two- and three-body electron attachment rates, τ, are also functions of the electric field strength and the air density and are also found using data from *Morrow and Lowke* [1997] and *Liu and Pasko* [2004]. In this work, the MSIS-E-90 atmospheric model is used to calculated air densities.

[63] The ionization rate, α, [electron-ion pairs per meter per runaway electron] is $8350\,\mathrm{m}^{-1} \times n$ as calculated by *Dwyer and Babich* [2011]. The speed of the runaway electron avalanches $\beta = v/c = 0.89$ as calculated by *Coleman and Dwyer* [2006]. All other symbols in this paper have their usual meaning.

[64] In the calculations presented below, we assume that the electric field in the avalanche region is in the $-z$ direction, resulting in only an azimuthal magnetic field. There exists some evidence that many TGFs have broad angular distributions of the runaway electrons [*Dwyer and Smith* 2005; *Gjesteland et al.* 2011], possibly indicating either diverging or converging electric field lines at the end of the avalanche region. We do not include non-vertical field lines here, although non-vertical field lines may be easily included by convolving equation (24) with the desired distribution. Even if non-vertical field lines are included, they will not significantly change the radiated azimuthal magnetic field component. Therefore, we present the azimuthal magnetic field below, which will remain approximately correct for diverging or converging electric field lines as well.

11. Predicted Characteristics of TGF Radio Emissions

[65] To illustrate the radial dependence of the RF waveforms, which will change due to the relative importance of the induction and radiation terms, we first present, in Figure 2, the azimuthal component of B produced by a TGF with no substructure, i.e., $N_p \to \infty$, at a radial distance of 100 km (solid curves) and at 500 km (dashed curves). We refer to this as model E in Table 2. The black curves are for a source altitude of 13 km, and the red curves are for an altitude of 17 km. For comparison, the curve 17 km has been normalized so that the first peak matches. The magnetic fields in Figure 2 are found by calculating the inverse Fourier transform of equation (26). The effects of the induction component are apparent in the two 100 km curves, with the drifting ions producing the long tails in the solid curves. Note the differences in the signals from the two TGF altitudes, which arise from the non-scaling law of the three-body attachment of low-energy electrons. Because the electric field is not modeled in this work, the exact shape and size of the ion tail seen in the figure should not be given too much weight.

[66] Figure 3 is the azimuthal component of dB/dt for a TGF for the four different models in Table 2 at $R_o = 500$ km and $\theta = \pi/2$: (A) the fast lightning source with $N_p = 30$, (B) slow lightning source with $N_p = 100$, (C) slow lightning source with $N_p = 10{,}000$, and (D) the relativistic feedback discharge model with $N_p = 10^{13}$. Note that model E, the idealized case with an infinite number of avalanche pulses,

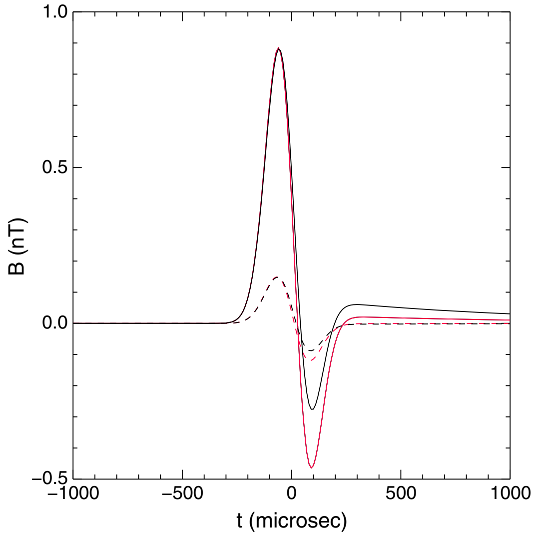

Figure 2. Magnetic field, B, produced by a TGF with no substructure, i.e., $N_p \to \infty$, at a radial distance of 100 km (solid curves) and at 500 km (dashed curves). The black curves are for a source altitude of 13 km, and the red curves are for an altitude of 17 km. For comparison, the curve 17 km have been normalized so that the first peak match.

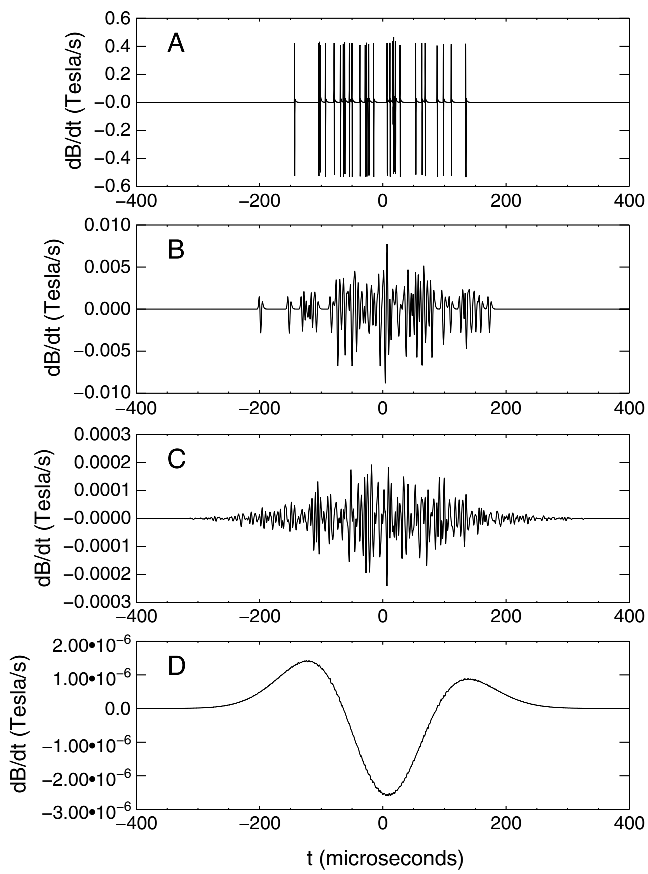

Figure 3. dB/dt at a radial distance of 500 km ($\theta = \pi/2$) for five TGF models. (a) Fast lightning source with $N_p = 30$. (b) Slow lightning source with $N_p = 100$. (c) Slow lightning source with $N_p = 10{,}000$. (d) Relativistic feedback discharge model with $N_p = 10^{13}$.

is almost indistinguishable from model D in this figure and so we do not plot it. We chose to present dB/dt rather than B, because dB/dt sensors are in common use [e.g., *Cummer et al.* 2011] and they are more sensitive to higher-frequency variations where the models differ. For these figures, the inverse Fourier transform of equations (24) and (25) were calculated. The avalanche pulses were chosen randomly from the probability distribution, f_{TGF}, as described in case 1 above. In other words, the figures show a possible realization of a TGF rather than an ensemble average. As can be seen, the models produce significantly different RF signatures that should be easily distinguishable. For the fast lightning source model, the RF signals are extremely large, resembling a rapid series of narrow pulses, but orders of magnitude larger than what are traditionally referred to as narrow bipolar pulses (NBPs) [*Le Vine* 1980; *Smith et al.* 1999]. We note that if the number of runaway electrons in the TGF were smaller, then the RF signals would also be smaller, but it is not clear if such a TGF would be detectable by spacecraft.

[67] Figure 4 shows the spectral energy density [electromagnetic energy per unit frequency interval per unit area], calculated from equation (32), for the different models at $R_o = 500$ km and $\theta = \pi/2$. In addition to the models shown in Figure 3, we also show the case where $N_p \to \infty$ (model E). In the figure, each curve has two humps: the lower frequency hump with a peak near 2000 Hz is due to the overall envelop of the TGF current waveform. The higher-frequency humps with peaks at 50 kHz or above are due to the currents from individual avalanche pulses.

[68] Figure 5 shows the spectral energy density for $N_p \to \infty$ (model E), calculated by equation (32), for several TGF durations, σ_{TGF}. Also shown are the bandwidths of WWLLN (dashed lines) and the continuously recorded bandwidth of the Stanford Palmer Station system (dotted lines). As can be seen, the shorter TGFs put significant RF energy into the sensitive frequency range of both WWLLN and Palmer Station.

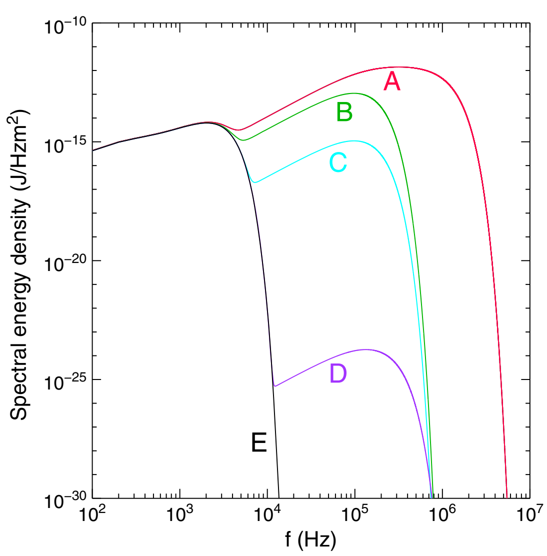

Figure 4. Spectral energy density per unit area (J/Hz m^2) for the electromagnetic radiation from the TGF at a radial distance of 500 km ($\theta = \pi/2$) for the four source models described in Figures 3 and Table 2, plus the $N_p \to \infty$ case (curve E).

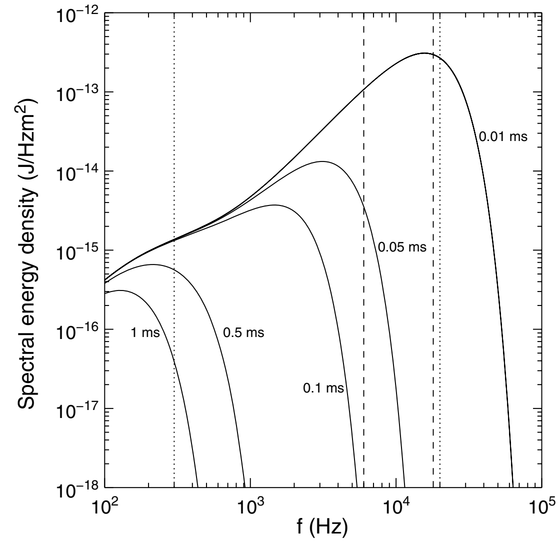

Figure 5. Spectral energy density per unit area (J/Hz m^2) for the electromagnetic radiation from the TGF at a radial distance of 500 km ($\theta = \pi/2$) for the five TGF durations for the $N_p \to \infty$ case. The vertical dotted lines show the bandwidth of Stanford's Palmer Station sferics receiver, and the vertical dashed lines show the bandwidth of WWLLN.

[69] The World Wide lightning location network (WWLLN) is optimized to measure lightning with a peak spectral energy density around 10 kHz. WWLLN's detectors record RF signals from 1 to 24 kHz, with data between 6 and 18 kHz contributing most to the analysis [*Hutchins et al.* 2012]. From Figure 5, the TGF will also produce an RF signal with substantial spectral energy density near 10 kHz, similar to lightning. Therefore, it is expected that the WWLLN would efficiently detect such short TGFs [*Dwyer* 2012]. Indeed, it is possible that radio pulses from TGFs may often be mistaken for lightning. From Figure 5, for models in which N_p is large, we would expect the detection efficiencies of TGFs to drop sharply as the duration of the TGF increases (assuming that WWLLN and Palmer Station are mostly detecting the TGF and not accompanying lightning). This decrease in the WWLNN detection efficiency of TGFs with increasing TGF duration has recently been reported by *Connaughton et al.* [2013].

12. Comparison to Measured TGF-Associated Radio Emissions

[70] There are numerous reports of TGF-associated radio emissions that span the entire ULF to LF radio bandwidth [*Cummer et al.* 2005; *Inan et al.* 2006; *Lu et al.* 2011; *Cummer et al.* 2011]. A quantitative comparison between measurements and predictions will provide some new and important constraints on the possible TGF source mechanisms and parameters. We focus here on a comparison with the LF radio data reported by *Cummer et al.* [2011], as the predictions in section 11 indicate that the differences between TGF mechanisms are clearest at frequencies around or above roughly 100 kHz. However, we first must address some practical radio propagation effects that are important in measurements for distances longer than roughly 100 km and also address the details of the sensor frequency response to ensure a meaningful direct comparison with predictions.

12.1. LF Ground-Wave Propagation

[71] The prediction-measurement comparison that follows focuses on the ground-wave component of the LF radiation during the TGF generation time window. This ensures that the more complicated ionospheric reflection effects do not complicate the effect of the source parameters in the signal. The amplitude of the ground-wave component suffers attenuation beyond the simple $1/r$ for radiation fields due to the spherical geometry and the imperfect conductivity of the air-ground interface. This extra attenuation, which is frequency dependent, strongly influences the observed VLF and LF signal at propagation distances beyond roughly 100 km and thus must be accounted for in the comparison.

[72] The behavior of this additional attenuation is conveniently summarized in an International Telecommunications Union Recommendation [ITU-R P.368-7, 2000]. Because this attenuation increases with increasing frequency, we can compute its impact on the waveform by treating it as a causal low-pass filter. For example, we find that cascaded first-order low-pass filters with cutoff frequencies of 150 and 500 kHz and a passband amplitude of 0.8 closely approximate the effect of the extra ground wave attenuation incurred over a 500 km propagation path over dry land. Since the measured waveforms used here were measured over roughly 500 km propagation paths, we apply this filter to the theoretical predictions described above (which include the $1/r$ radiation field attenuation) before making the comparison.

12.2. Sensor Frequency Response

[73] The frequency of the sensor response also influences the observed waveform and thus must be accounted for in a comparison between measurements and predictions. The sensor used by *Cummer et al.* [2011] is an orthogonal pair of ferrite-core magnetic field induction coils. These measure the two horizontal components of the radiated magnetic field. Using the NLDN geolocation of the events, these signals are combined through a vector rotation to yield a signal corresponding to the azimuthal magnetic field, which is the primary radiated component.

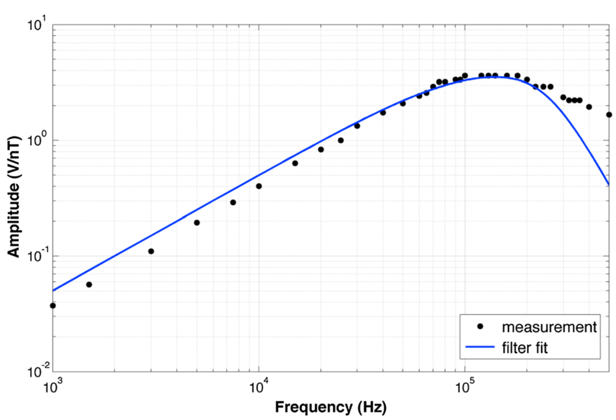

Figure 6. Measured laboratory sensitivity (black dots) versus frequency for the LF magnetic field coil. The blue line is a filter-based fit to the measurements that enables accurate modeling of the sensor response in calculations.

[74] The frequency response of this sensor was designed to emphasize LF frequencies to better distinguish fast in-cloud processes from conventional lightning discharges. To first order, the sensor has a response that is proportional

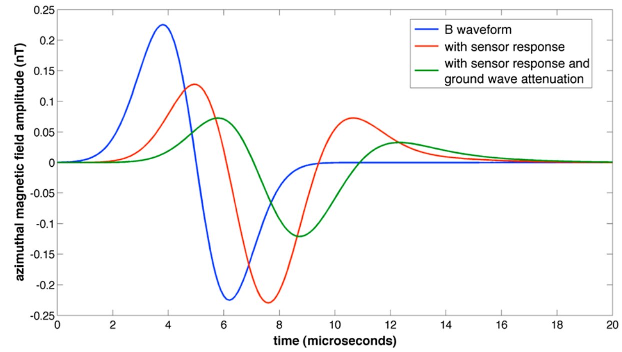

Figure 7. Computed azimuthal magnetic field waveforms for a fast (<3 μs FWHM) 1 C-km charge moment change observed at 500 km range. Blue: the radiated B waveform. Red: the measured waveform with the sensor frequency response applied. Green: the measured waveform with the sensor response and the ground-wave attenuation applied.

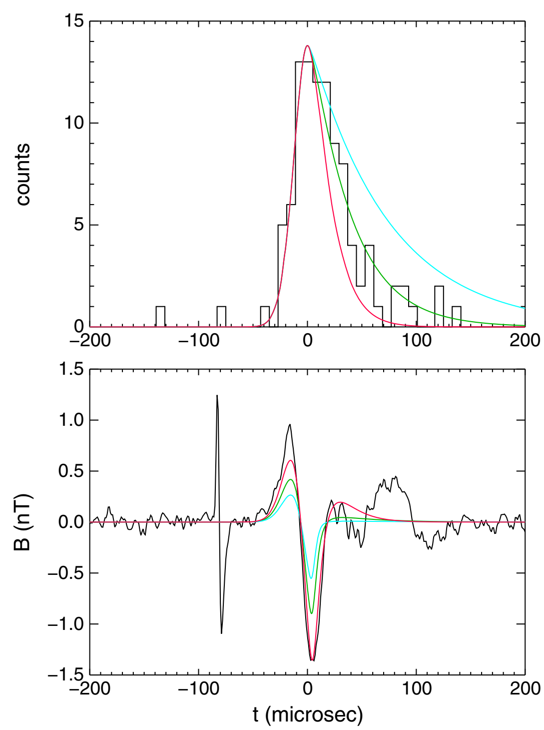

Figure 8. Top panel: Fermi counts versus time for the 3 August 2010 TGF (black) as presented in *Cummer et al.* [2011]. The smooth curves show different fits of equation (33). Because of Compton scattering, the source function may be most similar to the red curve. Bottom panel: The magnetic field measured by the Duke sensor at Florida Tech (black) for the same event. The smooth curves show the predicted RF emissions based upon the sources shown in the top panel. The models include the effects of propagation and the antenna response discussed in section 12.

to frequency (like a dB/dt sensor) from 0 to 100 kHz, and it has a frequency-independent response (like a B sensor) from 100 to 200 kHz. Above 200 kHz, the response drops sharply, and the signal is sampled at 1 MHz.

[75] Since the overall bandwidths of these two different responses are equal, there are two reasonable ways to present calibrated data. We prefer to consider this sensor a B sensor, and thus calibrated with magnetic field units, with a first-order high-pass response cutoff at 100 kHz. This ensures easier comparison with other direct measurements of electric and magnetic fields.

[76] Figure 6 shows lab measurements of the sensitivity of the coil and preamp made using a controlled field-generating source. This calibration was confirmed in field measurements through a cross calibration with at 1–20 kHz existing VLF sensors. Based on repeated measurements of multiple coils, this calibration is accurate to a level of $\pm 20\%$.

[77] To provide a sense of the impact of ground-wave attenuation and of the sensor frequency response on the measured waveforms, Figure 7 compares three computed magnetic field waveforms. One (blue) is the azimuthal magnetic field waveform produced at a range of 500 km by a 1 C charge transfer over a 1 km length driven by a Gaussian current pulse with a full width half maximum of 2.8 µs. Another (red) is the same but with the sensor frequency response applied. The last (green) includes both the sensor response and the ground-wave attenuation. Both of these effects alter the waveform significantly and thus must be (and is) accounted for in the comparison of measurements and data that follow in Section 12.3.

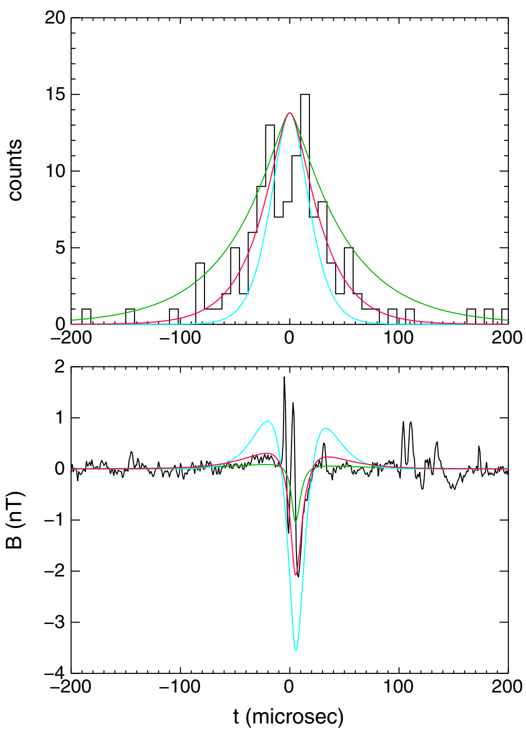

Figure 9. Top panel: Fermi counts versus time for the 5 September 2010 TGF (black) as presented in *Cummer et al.* [2011]. The smooth curves show different fits of equation (33). Bottom panel: The magnetic field measured by the Duke sensor at Florida Tech (black) for the same event. The smooth curves show the predicted RF emissions based upon the sources shown in the top panel. The models include the effects of propagation and the antenna response discussed in section 12.

12.3. Comparison With September and August Fermi TGFs

[78] In Figures 8–11, we present comparisons of simulations to specific TGF RF waveforms measured by the Duke LF sensor. We first compare the current function presented in equation (33) to the Fermi TGF count rates presented by *Cummer et al.* [2011] (top panels of Figures 8 and 9). We next calculate the expected signal measured by the Duke sensor, including the propagation effects and the antenna response, and plot the model ($N_p \to \infty$) along with the observed signals (bottom panels Figures 8 and 9). The 3 August 2010 TGF was 466.7 km from the LF sensor in Florida, and the 5 September 2010 TGF was 504.3 km from the same LF sensor. The model shows that reasonable fits to the TGF count rates give reasonable fits to the observed magnetic fields. The fits may be used to find the total path length of runaway electrons at the source, Ω. For the red curves in the top and bottom panels of Figures 8 and 9, we find that $\Omega = 1.5 \times 10^{20}$ m and $\Omega = 7.0 \times 10^{20}$ m for the August and September events, respectively. These values are about 1.75 and 8.0 times larger than the average TGF inference by RHESSI. The blue and green curves seen in those figures use the same Ω. The differences in the amplitudes seen in the bottom panels are due to the different current durations.

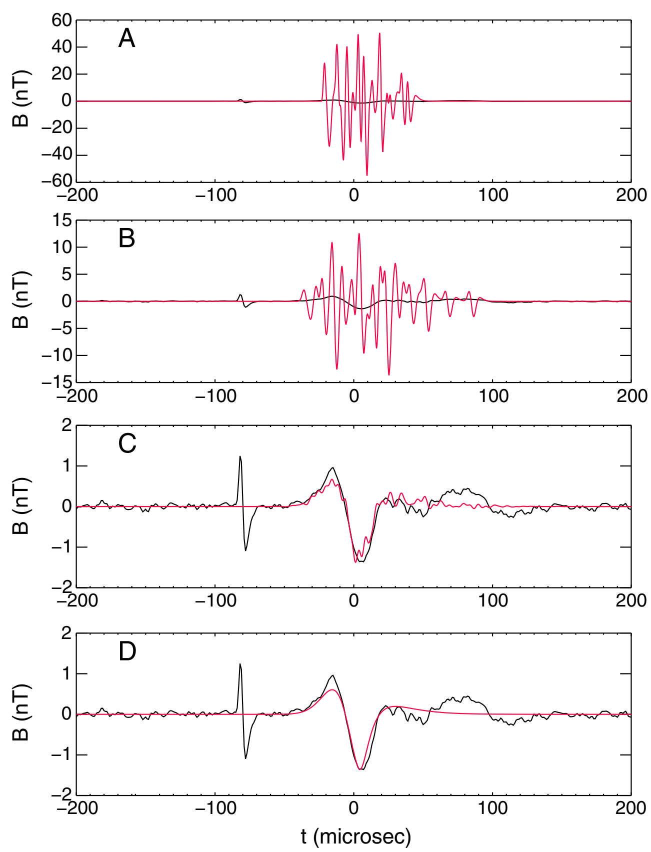

Figure 10. Fits of the different TGF models to the 3 August 2010 TGF.

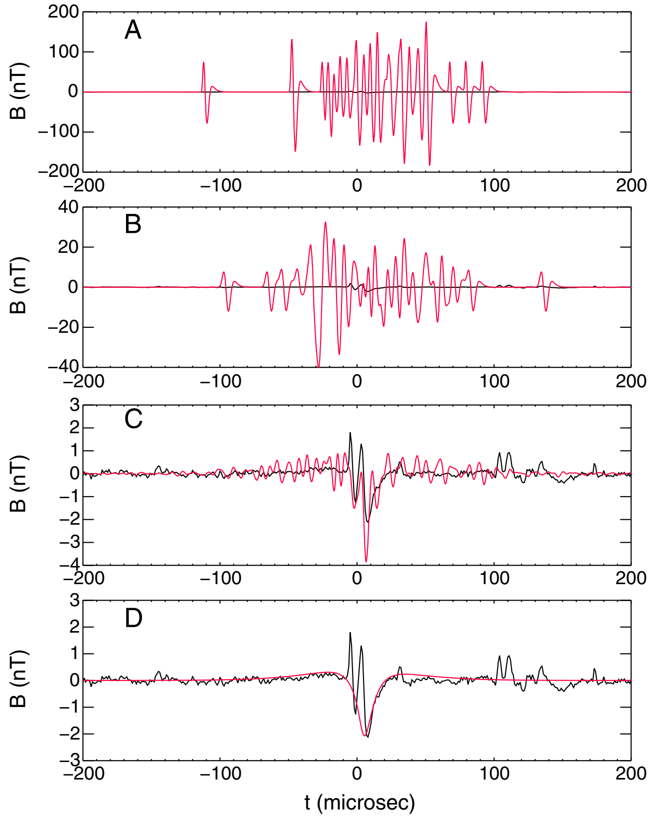

Figure 11. Fits of the different TGF models to the 5 September 2010 TGF.

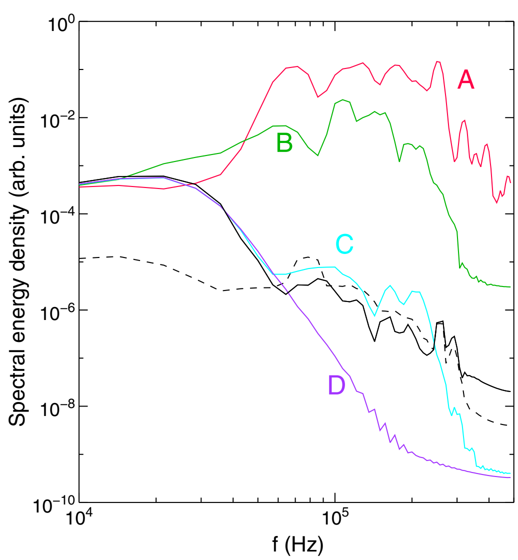

Figure 12. Spectral energy density per unit area (J/Hz m^2) for the electromagnetic radiation from the TGF at a radial distance of 500 km ($\theta = \pi/2$) for the source models along with the spectral energy density measured for the 3 August 2010 TGF (black). The black dashed line shows the background. For the models, the effects of propagation and antenna response are included and the TGF is assumed to have the same overall shape as shown in Figure 8.

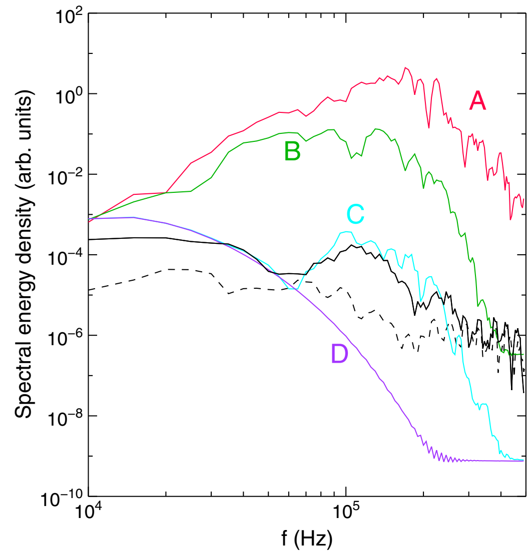

Figure 13. Spectral energy density per unit area (J/Hz m^2) for the electromagnetic radiation from the TGF at a radial distance of 500 km ($\theta = \pi/2$) for the source models along with the spectral energy density measured for the 5 September 2010 TGF (black). The black dashed line shows the background. For the models, the effects of propagation and antenna response are included and the TGF is assumed to have the same overall shape as shown in Figure 9.

[79] Figures 10 and 11 show the same fits (same Ω) as Figures 8 and 9 but for the different TGF models. As can be seen, the lightning leader models (models A–C) appears to greatly overpredict the amount of emission at higher frequencies because of the smaller number of seed particle (avalanche) pulses.

[80] This can be made more quantitative by comparing the spectral energy densities predicted by these models with that measured by for these TGFs (Figures 12 and 13). The plots in the two figures each show one possible realization of a TGF, which may be compared with the average spectral energy densities in Figure 4. As can be seen, the TGF must be made up of at least 10,000 seed particle pulses in order to be consistent with the emission measured near 100 kHz. In other words, for the models under consideration, consistency with the measurement requires either a very large (and perhaps unrealistic) number of leader steps (or leader current pulses) or a feedback-dominated discharge that naturally contains a very large number of seed particle injections.

13. Discussion

[81] In this paper, we have developed the theory of radio frequency emissions from terrestrial gamma-ray flashes. Furthermore, we have shown that the spectral energy density may be used to distinguish various TGF models. Because TGFs produce RF emissions that should be easily detectable, it may eventually be possible to study TGFs using electromagnetic sensors without the need for accompanying spacecraft gamma-ray observations.

[82] For a given source altitude, the peak electric current produced by the TGF is directly proportional to the number of runaway electrons at the source and inversely proportional

to the duration of the TGF. Hence, intrinsically brighter TGFs will produce larger current pulses. For typical TGF parameters, the peak current is on the order of 10 kA and could reach 100 kA for the shortest TGFs. Because the amplitude of the RF radiation is proportional to the derivative of the current moment, the amplitude of the RF pulse is approximately proportional to the inverse square of the duration of the TGF. As a result, shorter TGF should be much easier to detect at radio frequencies than longer ones. In addition, TGFs that are intrinsically weaker, producing fewer runaway electrons, will also produce smaller radio pulses.

13.1. Lightning Currents

[83] In the analysis presented in this paper, we do not include the RF emissions caused by the electrical currents directly associated with the lightning, i.e., the currents generated by the leaders and streamers associated with the IC lightning known to accompany the TGFs [*Shao et al.*, 2010; *Lu et al.*, 2010; *Cummer et al.*, 2011]. While many previous authors have considered such electrical currents from lightning [e.g., *Carlson et al.*, 2009; 2010; *Celestin et al.*, 2012], we emphasize that in this work, we are instead considering the electrical currents produced directly by the relativistic runaway electrons and their accompanying ionization. Nevertheless, the current pulses from the lightning channels are usually present and so should be considered. These currents may be very short and very large, especially according to work by Celestin *et al.* and Carlson, and so the spectral energy density at higher frequencies presented in this work may be greatly underestimated if these models are correct.

[84] According to *Uman* [2001], three kinds of intra-cloud lightning pulses have been previously identified: (1) trains of unipolar pulses with fast, $<0.2\,\mu$s rise times and a full width of about $0.75\,\mu$s [*Krider et al.*, 1979]; (2) large bipolar pulses with a mean full width of $63\,\mu$s [*Kitagawa and Brook* 1960; *Weidman and Krider* 1979]. These bipolar pulses often have several fast unipolar pulses superimposed on the initial peak. *Weidman and Krider* [1979] suggested that the fast pulses on the initial rise may be due to step-like breakdown currents. (3) Narrow bipolar pulses with fast microseconds rises and typical durations of 1–$20\,\mu$s [*Le Vine* 1980; *Smith et al.*, 1999]. Narrow bipolar pulses are some of the most powerful RF emitters from thunderstorms.

[85] The fast lightning processes seen in Figure 8 near time $-80\,\mu$s and in Figure 9 near times $0\,\mu$s and $100\,\mu$s appear to be consistent with the previously reported large bipolar pulses (number 2 above) and so may be associated with leader steps. *Cummer et al.* [2011] argued that these fast lightning processes do not appear to be directly related to the TGFs based on their random occurrence with respect to the TGF. If these lightning pulses happen to occur during the same time period as the TGF, then clearly their spectral energy density would add to that of the TGF itself. This appears to be the case for the 5 September 2010 TGF. In that event at time $0\,\mu$s, there are two fast pulses, which contribute to the spectral energy density at 100 kHz in Figure 13. However, these pulses are not present on the right side of the TGF pulse, as should occur if they were due to lightning leader models of TGFs, and so may be part of an unrelated process within the same storm.

[86] The relativistic feedback discharge model, which, on its own, puts little spectral energy density at higher frequencies, may also be accompanied by IC lightning that produces fast RF pulses [*Dwyer* 2012]. In addition, other background sources such as manmade sources will also contribute to the spectra energy density. As a result, the spectral energy densities, especially at higher frequencies, predicted for each model should be viewed as a lower limit. Therefore, a model that predicts a higher spectral energy density in a given band than is observed may be excluded. However, predicting a lower value cannot be used to rule out a model until all sources of background are fully understood.

13.2. Constraints on Models

[87] Even with the caveats mentioned just above, a meaningful limit may be put on the number of avalanche pulses occurring during a TGF using the published LF measurements. Based upon Figures 10–13 and B1, it appears that all models with less than about 10^4 avalanche pulses are inconsistent with measurements of these two TGFs. This can easily be seen in Figures 10 and 11, where the lightning leader models greatly over predict the higher-frequency component in the waveform. As mentioned earlier, *Carlson et al.* [2010] and *Celestin and Pasko* [2011] argued that TGFs are emitted by lightning inside thunderclouds and not near the ground because unlike lightning leaders near the ground, lightning leaders that make TGFs inside thunderclouds are not heavily branched. This argument does not appear to be consistent with results presented here, which reopens the following question: if lightning leaders make TGFs inside thunderclouds, then why do lightning leaders near the ground not produce similar gamma-ray emissions?

[88] Similarly, the number of avalanches generated by RREAs that have been seeded by atmospheric cosmic rays is also constrained to be more than 10^4 [*Carlson et al.*, 2008]. In other words, at least 10^4 cosmic-ray seed particles are required. In order to produce 10^{17} runaway electrons from 10^4 seed particles, an avalanche multiplication factor of 10^{13} is needed, which is about 7 orders of magnitude larger than the limit set by relativistic feedback. Such a large avalanche multiplication factor would also require an unphysically large potential difference in the avalanche region, and so the observations and analysis presented in this paper do not provide a new constraint on the RREA-cosmic-ray mechanism. However, with improved observations and the analysis presented here, it may be possible to test this mechanism in future work.

[89] Consider model A with $N_p = 30$. The peak magnetic field, B, for the pulses shown in Figure 11 is larger than 2×10^{-6} T at a distance of about 500 km. At 100 km, this would give a peak magnetic field of more than 1×10^{-5} T. For a wave propagating in the $\hat{n} = \vec{R}_o / R_o$ direction, the radiation electric field (in V/m) can be found from the radiation magnetic field from

$$\vec{E}_{\text{rad}} = -c\hat{n} \times \vec{B}_{\text{rad}}. \tag{37}$$

This gives a peak radiation electric field of more than 3000 V/m at 100 km. This value may be compared with the peak field of 10–100 V/m typically seen from narrow bipolar events (NBE) at that distance, which are some of the largest radio pulses seen from thunderclouds. Furthermore, as discussed in section B and shown in Figure B1, the peak currents for this model are very large, exceeding 1×10^6 A. Such current pulses would be some of the largest produced in our atmosphere. If sequences of pulses with this size were produced by TGFs, it would be extremely surprising if they had not been reported already, independent of TGF observations. As mentioned above, a smaller number of runaway electrons, or a smaller values of Ω, would result in smaller current pulses, but decreasing the number of runaway electrons or Ω too much would be inconsistent with TGF gamma-ray fluence measurements.

[90] If each avalanche pulse is assumed to come from a lightning leader step, or a large and fast current pulse along a lightning channel, then 10,000 of these occurring in less than 100 μs does not seem physical, for describing either the number of lightning branches or the number of current pulses along a single channel. Indeed, LMA observations of upward lightning during the early phase do not suggest heavily branched channels [*Lu et al.*, 2010]. Because the characterizing feature of the Celestin, Xu, and Pasko model is a small number of very intense pulses, we consider the current work to be inconsistent with that model, at least for these two events. On the other hand, the relativistic feedback discharge model, which predicts an RF pulse with a smooth profile, is consistent with the observations.

13.3. Streamer Model

[91] An alternative scenario that may also be consistent with the observations is each avalanche pulse is not emitted by a lightning leader but is instead emitted by an individual streamer [e.g., *Moss et al.*, 2006; *Celestin and Pasko* 2011]. For instance, one might imagine that the pulses of runaway electrons observed near the ground ($\sigma_s \sim 0.2$ μs) are really the superposition of many fast sources, such as from a large number of streamers emitted during the coronal flash of a lightning leader step. Inside a thundercloud, where the ambient field may be above the minimum streamer propagation field, the streamers in the coronal flash could conceivably keep propagating over a large distance. In this scenario, the $\sigma_s \sim 0.2$ μs pulse seen near the ground becomes the entire $\sigma_{\mathrm{TGF}} \sim 100$ μs duration a TGF, and the individual sources (streamer emissions) might better be described by the fast lightning source timescale. The runaway electrons might then be emitted intermittently, say, as the streamers branch. A TGF then is similar to one leader step seen on the ground; the duration is lengthened not by Compton scattering of the gamma rays but by the longer propagation time of the streamers. Each avalanche pulse is associated not with a leader step but with a current pulse associated with one of many streamers. Because there may be a large number of streamers for each leader, this would help explain the lack of emission in the few hundred kilohertz range. While detailed modeling is still needed, one might expect more VHF emission compared with the relativistic feedback discharge model.

13.4. Observations at Small Angles

[92] The examples presented in this paper have mainly considered observations at large distances with observation angles close to 90° from the beam direction. We note that the RF waveforms will differ at closer distances and other angles. In particular, at smaller angles, relativistic beaming, which enters the equations above through the term $(1 - \beta \cos\theta)$, will enhance the higher-frequency component compared with larger angles. Also, because the runaway electron avalanches have a speed $\beta = v/c = 0.89$, at small angles, the radio emission from a conventional discharge with $\beta << 1$ will have significantly less higher frequency emission than the relativistic case. By performing multipoint observations, it may be possible to distinguish pulses emitted by runaway electron avalanches from conventional breakdown.

13.5. Relativistic Feedback Discharges

[93] We end with a brief discussion of the implications for the relativistic feedback discharge mechanism. This work strongly supports the possibility first raised by *Cummer et al.* [2011] that the TGF-simultaneous LF pulses are produced by the electron acceleration process itself and also confirms the predictions of *Dwyer* [2012] that the mechanism that produces TGFs also produce some of the most powerful electrical discharges (highest peak current moments) inside thunderstorms. If the TGFs are produced by high field runaway by lightning leaders, then this discharge could be considered to be an extension of the lightning. On the other hand, if TGFs are byproducts of relativistic feedback discharges, then they may only be loosely connected to lightning processes within the thundercloud and could in principle occur without lightning. Relativistic feedback rapidly discharges large regions of the thundercloud, with lightning-like currents, and so may be easily mistaken for lightning when recorded in radio waves. However, because relativistic feedback discharges do not involve a hot leader channel, they will emit little visible light compared to normal lightning. As a result, relativistic feedback discharges may be a form of "dark lightning," appearing as large lightning discharges in radio waves but emitting almost no detectable light.

Appendix A : Calculations Involving Fluctuations

[94] Consider the function that appears in equation (25):

$$g(\omega) = \sum_j a_j \exp(i\omega t_j), \tag{A1}$$

where $\sum_j a_j = 1$.

[95] For case 1, described above, for which each avalanche pulse produces the same number of runaway electrons, we have

$$g(\omega) = \frac{1}{N_p} \sum_{j=1}^{N_p} \exp(i\omega\ t_j). \tag{A2}$$

[96] The times, t_j, are drawn randomly from the normalized distribution function, $f_{\mathrm{TGF}}(t)$, that describes the time-intensity of the TGF at the source.

[97] Let us first consider the finite time interval from $-T$ to T, containing the TGF. We divide this interval into a number of small sub-intervals of duration, Δt. Then in the kth sub-interval, the ensemble average number of avalanche pulses

is $\langle n_k \rangle = N_p f(t_k) \Delta t$. As a result, the ensemble average of the function g is

$$\langle g(\omega) \rangle = \frac{1}{N_p} \sum_k N_p f_{\rm TGF}(t_k) \Delta t \exp(i\omega \ t_k), \tag{A3}$$

where the summation is now over all sub-intervals, rather than over all avalanche pulses as in equations (A1) and (A2). In the limit that $\Delta t \to 0$,

$$\langle g(\omega) \rangle = \int_{-T}^{T} f_{\rm TGF}(t) \exp(i\omega t) dt. \tag{A4}$$

[98] Letting $T \to \infty$, we have

$$\langle g(\omega) \rangle = \int_{-\infty}^{\infty} f_{\rm TGF}(t) \exp(i\omega t) dt = \sqrt{2\pi} \tilde{f}_{\rm TGF} \tag{A5}$$

[99] For a specific TGF, let us write $g(\omega) = \langle g(\omega) \rangle + dg(\omega)$, where

$$dg(\omega) = \frac{1}{N_p} \sum_k dn_k \exp(i\omega t_k), \tag{A6}$$

with $dn_k = n_k - \langle n_k \rangle$ and n_k being the actual number of avalanche pulses in the kth sub-interval for that TGF. Note that $\langle dn_k \rangle = 0$, since it represents a fluctuation around the average. Although the average of the fluctuations vanishes, the RMS does not, and it is the RMS that enters into the spectral energy density of the electromagnetic field.

[100] The RMS of g is

$$\left\langle |g|^2 \right\rangle = \left\langle |\langle g \rangle + dg|^2 \right\rangle = |\langle g \rangle|^2 + \left\langle |dg|^2 \right\rangle, \tag{A7}$$

where $|g|^2 = gg^*$. We have used the fact that $\langle \langle g \rangle \ dg^* \rangle = \langle \langle g^* \rangle \ dg \rangle = 0$.

$$\left\langle |dg(\omega)|^2 \right\rangle = \frac{1}{N_p^2} \sum_k \sum_l \langle dn_k dn_l \rangle \exp(i\omega(t_k - t_l)). \tag{A8}$$

[101] Because the fluctuations are assumed to be uncorrelated between sub-intervals, only the terms with $k = l$ are nonzero. As a result,

$$\left\langle |dg(\omega)|^2 \right\rangle = \frac{1}{N_p^2} \sum_k \langle dn_k^2 \rangle. \tag{A9}$$

[102] In each sub-interval, the number, n_k, follows Poisson counting statistics, so that $\langle dn_k^2 \rangle = \langle n_k \rangle$. Therefore,

$$\langle dn_k^2 \rangle = N_p f(t_k) \Delta t, \tag{A10}$$

which gives

$$\left\langle |dg(\omega)|^2 \right\rangle = \frac{1}{N_p} \sum_k f(t_k) \Delta t. \tag{A11}$$

[103] In the limit that $\Delta t \to 0$,

$$\left\langle |dg(\omega)|^2 \right\rangle = \frac{1}{N_p} \int_{-T}^{T} f(t) \ dt. \tag{A12}$$

[104] Letting $T \to \infty$, we have

$$\left\langle |dg(\omega)|^2 \right\rangle = \frac{1}{N_p} \int_{-\infty}^{\infty} f(t) \ dt = \frac{1}{N_p}, \tag{A13}$$

since f is a normalized function.

[105] Therefore,

$$\left\langle |g(\omega)|^2 \right\rangle = 2\pi \tilde{f}_{\rm TGF}^2 + \frac{1}{N_p}. \tag{A14}$$

[106] For the case where $f_{\rm TGF}$ is a Gaussian distribution

$$f_{\rm TGF}(t) = \frac{1}{\sqrt{2\pi\sigma_{\rm TGF}^2}} \exp\left(\frac{-t^2}{2\sigma_{\rm TGF}^2}\right), \tag{A15}$$

then

$$\left\langle |g(\omega)|^2 \right\rangle = \exp\left(-\omega^2 \sigma_{\rm TGF}^2\right) + \frac{1}{N_p}. \tag{A16}$$

[107] A similar calculation may be done for case 2, for which the avalanche pulses occur at a constant rate, r, and the number of runaway electrons in the avalanche pulses follow the function, $f_{\rm TGF}(t)/r$, where $f_{\rm TGF}$ is a normalized function determined by time-intensity profile of the TGF. We find that equation (A14) also holds for case 2 as long as the number of avalanche pulses is defined as $N_p = r\,\Delta T$, with

$$\Delta T = \left[\int_{-\infty}^{\infty} f_{\rm TGF}^2 \ dt \right]^{-1}. \tag{A17}$$

[108] If $f_{\rm TGF}$ is a Gaussian function, then equation (A17) gives $\Delta T = 2\sqrt{\pi}\sigma_{\rm TGF}$. In other words, for a constant rate of avalanche pulses, equation (A14) may be used if N_p is defined to be the number of avalanches that occur in the time period that contains 92% of the TGF runaway electrons.

[109] In summary, equation (A14), which is also given in equation (28) and used thereafter, may be used for both cases considered in this paper. In reality, it is likely that avalanche pulses in a TGF will both vary in size and occur at non-constant rates. However, because the two cases considered above represent the two extremes, i.e., constant size and constant rate, and equation (A14) applies to both, it is reasonable to use equation (A14) for TGFs in general.

Appendix B : Electric Currents

[110] In this appendix, we calculate the current moment at the source. The current moment (A m) is

$$\vec{I}_{re}(t) = \int_{-\infty}^{\infty} \int_{-\infty}^{\infty} \int_{-\infty}^{\infty} \vec{J}_{re}(x, y, z, t) \, dxdydz. \tag{B1}$$

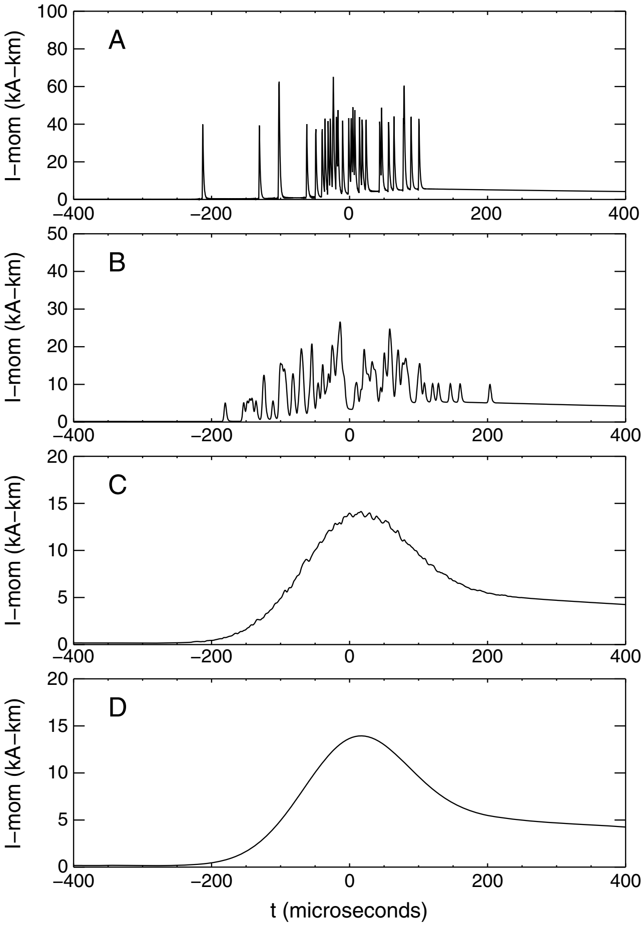

Figure B1. Electrical current moments versus time for the TGF models shown in Figure 3.

[111] As is section 4, we shall define the +z direction to be the runaway avalanche direction, keeping in mind that the avalanche could point in any direction with respect to vertical. Inserting equation (6) into equation (B1) gives

$$\overrightarrow{I}_{re}(t) = -ev\exp(\xi)\exp\left(\frac{-v^2t^2}{2\kappa^2}\right)\hat{z}. \tag{B2}$$

[112] Following the derivations presented in sections 2–5, the total current moment of the jth avalanche pulse is

$$\overrightarrow{I_j} = \overrightarrow{I}_{re}\circ \mathsf{s}_{\mathsf{j}}^{\text{seed}} + \left(\overrightarrow{\mathsf{I}}_{re}\circ \mathsf{s}_{\mathsf{j}}^{\text{seed}}\right)\circ(\mathsf{G}_{\text{ions}} + \mathsf{G}_{le}), \tag{B3}$$

where G_{le} and G_{ions}, given in equations (8) and (10), describe the contribution from low-energy electron and ions, and the open circle signifies the convolution with respect to time. Equation (B3) may be calculated directly, or the Fourier transform may be found:

$$\begin{aligned}\overrightarrow{\widetilde{I}}_j(\omega) &= \sqrt{2\pi}\,\overrightarrow{\widetilde{I}}_{re}(\omega)\ \widetilde{s}_j^{\text{seed}}(\omega)\\ &+ 2\pi\left(\overrightarrow{\widetilde{I}}_{re}(\omega)\widetilde{s}_j^{\text{seed}}(\omega)\right)\left(\widetilde{G}_{\text{ions}}(\omega) + \widetilde{G}_{le}(\omega)\right).\end{aligned} \tag{B4}$$

[113] The Fourier transform of equation (B2) is

$$\overrightarrow{\widetilde{I}}_{re}(\omega) = -e\kappa\exp(\xi)\exp\left(\frac{-\omega^2\kappa^2}{2v^2}\right)\hat{z}. \tag{B5}$$

[114] Plugging equations (B5) and (20)–(22) into equation (B4) gives

$$\overrightarrow{\widetilde{I}}_j(\omega) = \overrightarrow{\widetilde{I}^o}(\omega)\,N_j^{re}\exp\left(i\omega t_j\right), \tag{B6}$$

where

$$\begin{aligned}\overrightarrow{\widetilde{I}^o}(\omega) &= -\hat{z}\,e\,\kappa\exp\left(\frac{-\omega^2\left[\sigma_s^2 + (\kappa^2/v^2)\right]}{2}\right)\\ &\times\left\{1 + E\alpha\left(\mu_e - \mu_-\left(1 - \frac{\tau}{\tau_{\text{ion}}}\right)^{-1}\right)\left(\frac{1}{\tau} - i\omega\right)^{-1}\right.\\ &\left.+E\alpha\left(\mu_+ + \mu_-\left(1 - \frac{\tau}{\tau_{\text{ion}}}\right)^{-1}\right)\left(\frac{1}{\tau_{\text{ion}}} - i\omega\right)^{-1}\right\}.\end{aligned} \tag{B7}$$

[115] The total current moment is them the sum of all avalanche pulses

$$\begin{aligned}\overrightarrow{\widetilde{I}}_{\text{total}}(\omega) &= \overrightarrow{\widetilde{I}^o}(\omega)\sum_j N_j^{re}\exp\left(i\omega t_j\right)\\ &= \overrightarrow{\widetilde{I}^o}(\omega)\,N_{\text{TGF}}\sum_j a_j\exp\left(i\omega t_j\right),\end{aligned} \tag{B8}$$

where $a_j = N_j^{re}/N_{\text{TGF}}$ and N_{TGF} is the number of runaway electrons in the TGF, as in equation (25). The summation in equation (B6) may be calculated as in sections 7 and A. Figure B1 shows the current moments for the models shown in Figure 3–5. The current moment for model A, in the top panel of the figure, exceeds 50 kA km. Since this current moment is over a vertical distance of 50 m in this model, that gives a peak current larger than 1 million amps, even without adding in the lightning leader currents assumed by this model. Clearly, this is a very large current.

[116] The fluctuations in the current due to the finite number of avalanche pulses can be seen in the two middle panels. Since the radiation magnetic field is proportional to the derivative of the current moment, these fluctuations are amplified in the field.

[117] **Acknowledgments.** This work has been supported in part by DARPA grant HR0011-1-10-1-0061.

References

Briggs, M. S., et al. (2010), A first results on terrestrial gamma ray flashes from the Fermi Gamma-ray Burst Monitor, *J. Geophys. Res.*, *115*(A7), A07323.
Carlson, B., N. Lehtinen, and U. Inan (2007), Constraints on terrestrial gamma-ray flash production derived from satellite observations, *Geophys. Res. Lett.*, *34*(8), L08809.
Carlson, B., N. Lehtinen, and U. S. Inan (2008), Runaway relativistic electron avalanche seeding in the Earth's atmosphere, *J. Geophys. Res. 113*, A10307.
Carlson, B., N. Lehtinen, and U. Inan (2009), Terrestrial gamma ray flash production by lightning current pulses, *J. Geophys. Res. 114*, A00E08.
Carlson, B., N. Lehtinen, and U. Inan (2010), Terrestrial gamma ray flash production by active lightning leader channels, *J. Geophys. Res. 115*(A10), A10324.

Celestin, S., and V. Pasko (2011), Energy and fluxes of thermal runaway electrons produced by exponential growth of streamers during the stepping of lightning leaders and in transient luminous events, *J. Geophys. Res 116*, A03315.
Celestin, S., and V. Pasko (2012), Compton scattering effects on the duration of terrestrial gamma-ray flashes, *Geophys. Res. Lett.*, *39*, L02802, doi:10.1029/2011GL050342.
Celestin, S., W. Xu, and V. Pasko (2012), Terrestrial gamma ray flashes with energies up to 100 MeV produced by nonequilibrium acceleration of electrons in lightning, *J. Geophys. Res.*, *117*, A05315, doi:10.1029/2012JA017535.
Cobine, J. D. (1941), Gaseous Conductors, 1st ed., McGraw-Hill, New York and London.
Cohen, M. B., U. S. Inan, and G. J. Fishman (2006), Terrestrial gamma ray flashes observed aboard the Compton Gamma Ray Observatory/Burst and Transient Source Experiment and ELF/VLF radio atmospherics, *J. Geophys. Res.*, *111*(D24), D24109.
Cohen, M. B., U. S. Inan, R. K. Said, and T. Gjestland (2010), Geolocation of terrestrial gamma-ray flash source lightning, *Geophys. Res. Lett.*, *37*(2), L02801.
Coleman, L. M., and J. R. Dwyer (2006), The propagation speed of runaway electron avalanches, *Geophys. Res. Lett.*, *33*, L11810, doi:10.1029/2006GL025863.
Connaughton, V., et al. (2010), Associations between Fermi Gamma-ray Burst Monitor terrestrial gamma ray flashes and sferics from the World Wide Lightning Location Network, *J. Geophys. Res.*, *115*(A12), A12307.
Connaughton, V., et al. (2013), Radio signals from electron beams in Terrestrial Gamma-ray Flashes, *J. Geophys. Res.*, doi:10.1029/2012JA018288, in press.
Cummer, S. A., Y. Zhai, W. Hu, D. M. Smith, L. I. Lopez, and M. A. Stanley (2005), Measurements and implications of the relationship between lightning and terrestrial gamma ray flashes, *Geophys. Res. Lett.*, *32*, L08811, doi:10.1029/2005GL022778.
Cummer, S. A., G. Lu, M. S. Briggs, V. Connaughton, S. Xiong, G. J. Fishman, and J. R. Dwyer (2011), The lightning-TGF relationship on microsecond timescales, *Geophys. Res. Lett.*, *38*, L14810, doi:10.1029/2011GL048099.
Dwyer, J. R. (2003), A fundamental limit on electric fields in air, *Geophys. Res. Lett.*, *30*, 2055.
Dwyer, J. R. (2004), Implications of x-ray emission from lightning, *Geophys. Res. Lett.*, *31*, L12102, doi:10.1029/2004GL019795.
Dwyer, J. R. (2005), The initiation of lightning by runaway air breakdown, *Geophys. Res. Lett.*, *32*, L20808, doi:10.1029/2005GL023975.
Dwyer, J. R. (2007), Relativistic breakdown in planetary atmospheres, *Physics of Plasmas*, *14*(4), 042901-042901-17.
Dwyer, J. R. (2008), The source mechanisms of Terrestrial Gamma-ray Flashes (TGFs), *J. Geophys. Res.*, *113*(D10), D10103.
Dwyer, J. R. (2012), The relativistic feedback discharge model of terrestrial gamma ray flashes, *J. Geophys. Res.*, *117*, A02308, doi:10.1029/2011JA017160.
Dwyer, J. R., and L. Babich (2011), Low-energy electron production by relativistic runaway electron avalanches in air, *J. Geophys. Res.*, *116*, A09301, doi:10.1029/2011JA016494.
Dwyer, J. R., and D. M. Smith (2005), A comparison between Monte Carlo simulations of runaway breakdown and terrestrial gamma-ray flash observations, *Geophys. Res. Lett.*, *32*, L22804, doi:10.1029/2005GL023848.
Dwyer, J. R., et al. (2003), Energetic radiation produced during rocket-triggered lightning, *Science*, *299*, 694–697.
Dwyer J. R., et al. (2004), Measurements of X-ray emission from rocket-triggered lightning, *Geophys. Res. Lett.*, *31*, L05118, doi:10.1029/2003GL018770.
Dwyer, J. R., et al. (2005), X-ray bursts associated with leader steps in cloud-to-ground lightning, *Geophys. Res. Lett.*, *32*, L01803, doi:10.1029/2004GL021782.
Dwyer, J. R., M. A. Uman, and H. K. Rassoul (2009), The remote measurement of thunderstorm electrostatic fields, *J. Geophys. Res.*, *114*, D09208, doi:10.1029/2008JD011386.
Dwyer, J. R., D. M. Smith, M. A. Uman, Z. Saleh, B. Grefenstette, B. Hazelton, and H. K. Rassoul (2010), Estimation of the fluence of high-energy electron bursts produced by thunderclouds and the resulting radiation doses received in aircraft, *J. Geophys. Res.*, *115*(D9), doi:10.1029/2009JD012039.
Fishman, G. J., et al. (1994), Discovery of intense gamma-ray flashes of atmospheric origin, *Science*, *264*, 1313.
Fishman, G. J., et al. (2011), Temporal properties of the terrestrial gamma-ray flashes from the Gamma-Ray Burst Monitor on the Fermi Observatory, *J. Geophys. Res.*, *116*, A07304, doi:10.1029/2010JA016084.
Gjesteland, T., N. Østgaard, A. B. Collier, B. E. Carlson, M. B. Cohen, and N. G. Lehtinen (2011), Confining the angular distribution of terrestrial gamma ray flash emission, *J. Geophys. Res.*, *116*, A11313, doi:10.1029/2011JA016716.
Grefenstette, B. W., D. M. Smith, J. R. Dwyer, and G. J. Fishman (2008), Time evolution of terrestrial gamma ray flashes, *Geophys. Res. Lett.*, *35*(6), L06802.
Griffiths, D. J. (1999), Introduction to Electrodynamics, 3rd ed., Prentice Hall, Upper saddle River, New Jersey.
Gurevich, A. V. (1961), On the theory of runaway electrons, *Soviet Physics JETP*, *12*(5), 904–912.
Gurevich, A. V., G. M. Milikh, and R. A. Roussel-Dupré (1992), Runaway electron mechanism of air breakdown and preconditioning during a thunderstorm, *Phys. Lett. A*, *165*, 463.
Gurevich, A. V., K. P. Zybin, and Y. V. Medvedev (2007), Runaway breakdown in strong electric field as a source of terrestrial gamma flashes and gamma bursts in lightning leader steps, *Phys. Lett. A 361*, 119–125.
Hill, J. D., M. A. Uman, D. M. Jordan, J. R. Dwyer, and H. Rassoul (2012), "Chaotic" dart leaders in triggered lightning: Electric fields, X-rays, and source locations, *J. Geophys. Res.*, *117*, D03118, doi:10.1029/2011JD016737.
Howard, J., M. A. Uman, J. R. Dwyer, D. Hill, C. Biagi, Z. Saleh, J. Jerauld, and H. K. Rassoul (2008), Co-location of lightning leader X-ray and electric field change sources, *Geophys. Res. Lett.*, *35*(13), L13817.
Howard, J., M. Uman, C. Biagi, D. Hill, J. Jerauld, V. A. Rakov, J. Dwyer, Z. Saleh, and H. Rassoul (2010), RF and X-ray source locations during the lightning attachment process, *J. Geophys. Res.*, doi:10.1029/2009JD012055.
Hutchins, M. L., R. H. Holzworth, C. J. Rodger, and J. B. Brundell (2012), Far-field power of lightning strokes as measured by the World Wide Lightning Location Network, *J. Atmos. Oceanic Technol.*, *29*, 1102–1110.
Inan, S. U., S. C. Reising, G. J. Fishman, and J. M. Horack (1996), On the association of terrestrial gamma-ray bursts with lightning and implications for sprites, *Geophys. Res. Lett.*, *23*, 1017–1020.
Inan, U. S., M. B. Cohen, R. K. Said, D. M. Smith, and L. I. Lopez (2006), Terrestrial gamma ray flashes and lightning discharges, *Geophys. Res. Lett.*, *33*, L18802, doi:10.1029/2006GL027085.
International Telecommunication Union (2000), Ground-wave propagation curves for frequencies between 10 kHz and 30 MHz, Recommendation ITU-R P.368-7.
Jacobson, A. R., R. Holzworth, J. Harlin, R. Dowden, and E. Lay (2006), Performance assessment of the world wide lightning location network (WWLLN), using the Los Alamos sferic array (LASA) as ground truth, *J. Atmos. Oceanic Technol.*, *23*, 1082–1092, doi:10.1175/JTECH1902.1.
Kitagawa, N. and M. Brook (1960), A comparison of intracloud and cloud-to-ground lightning discharges, *J. Geophys. Res. 65*, 1189–1201.
Krider, E. P., C. D. Weidman, and D. M. LeVine (1979), The temporal structure of the HF and VHF radiation produced by intracloud lightning discharges, *J. Geophys. Res. 74*, 5760–5762.
Le Vine, D. M. (1980), Sources of the strongest RF radiation from lightning, *J. Geophys. Res. 85*, 4091–4095.
Lehtinen, N. G., T. F. Bell, and U. S. Inan (1999), Monte Carlo simulation of runaway MeV electron breakdown with application to red sprites and terrestrial gamma ray flashes. *J. Geophys. Res. 104*, 24699–24712.
Liu, N., and V. P. Pasko (2004), Effects of photoionization on propagation and branching of positive and negative streamers in sprites, *J. Geophys. Res.*, *109*, A04301, doi:10.1029/2003JA010064.
Lu, G., R. J. Blakeslee, J. Li, D. M. Smith, X.-M. Shao, E. W. McCaul, D. E. Buechler, H. J. Christian, J. M. Hall, and S. A. Cummer (2010), Lightning mapping observation of a terrestrial gamma-ray flash, *Geophys. Res. Lett.*, *37*(11), L11806.
Lu, G., S. A. Cummer, J. Li, F. Han, D. M. Smith, and B. W. Grefenstette (2011), Characteristics of broadband lightning emissions associated with terrestrial gamma ray flashes, *J. Geophys. Res.*, *116*(A3), A03316.
Marisaldi, M., et al. (2010), Detection of terrestrial gamma ray flashes up to 40 MeV by the AGILE satellite, *J. Geophys. Res.*, *115*, A00E13, doi:10.1029/2009JA014502.
Moore, C. B., K. B. Eack, G. D. Aulich, and W. Rison (2001), Energetic radiation associated with lightning stepped-leaders, *Geophys. Res. Lett.*, *28*, 2141–2144.
Morrow, R., and J. J. Lowke (1997), Streamer propagation in air, *J. Phys. D: Appl. Phys.*, *30*, 614–627.
Moss, G. D., V. P. Pasko, N. Liu, and G. Veronis (2006), Monte Carlo model for analysis of thermal runaway electrons in streamer tips in transient luminous events and streamer zones of lightning leaders, *J. Geophys. Res.*, *111*(A2), A02307.
Rodger, C. J., J. B. Brundell, R. H. Holzworth, and E. H. Lay (2009), Growing detection efficiency of the world wide lightning location network, in Coupling of Thunderstorms and Lightning Discharges to Near-Earth Space, edited by N. B. Crosby, T.-Y. Huang, and M. J. Rycroft, AIP Conf. Proc., vol. *1118*, pp. 15–20, Corte, France.

Saleh, Z., J. Dwyer, J. Howard, M. Uman, M. Bakhtiari, D. Concha, M. Stapleton, D. Hill, C. Biagi, and H. Rassoul (2009), Properties of the X-ray emission from rocket-triggered lightning as measured by the Thunderstorm Energetic Radiation Array (TERA), *J. Geophys. Res.*, *114*, D17, doi:10.1029/2008JD011618.

Schaal, M. M., J. R. Dwyer, Z. H. Saleh, H. K. Rassoul, M. A. Uman, J. D. Hill, and D. M. Jordan (2012), Spatial and energy distributions of X-ray emission from natural and rocket triggered lightning using measurements from the Thunderstorm Energetic Radiation Array (TERA), *J. Geophys. Res.*, *117*(D15), doi:10.1029/2012JD017897, in press.

Shao, X.-M., T. Hamlin, and D. M. Smith (2010), A closer examination of terrestrial gamma-ray flash-related lightning processes, *J. Geophys. Res.*, *115*(9), A00E30.

Smith, D. A., X. M. Shao, D. N. Holden, C. T. Rhodes, M. Brook, P. R. Krehbiel, M. Stanley, W. Rison, and R. J. Thomas (1999), A distinct class of isolated intracloud lightning discharges and their associated radio emissions, *J. Geophys. Res. 104*, 4189–4212.

Smith, D. M., L. I. Lopez, R. P. Lin, and C. P. Barrington-Leigh (2005), Terrestrial gamma-ray flashes observed up to 20 MeV, *Science*, *307*, 1085–1088.

Stanley, M., et al. (2006), Link between terrestrial gamma-ray flashes and intra-cloud lightning discharges, *Geophys. Res. Lett.*, *33*(6), L06803.

Tavani, M., et al. (2011), Terrestrial gamma-ray flashes as powerful particle accelerators, *Phys. Rev. Lett.*, *106*(1), 018501.

Uman, M. A. (2001), The Lightning Discharge, Dover Publications, Inc. Mineola, New York.

Weidman, C. D., and E. P. Krider (1979), The radiation fields wave forms produced by intracloud lightning discharge processes, *J. Geophys. Res.*, *84*, 3159–3164.

Wilson, C. T. R. (1925), The acceleration of beta-particles in strong electric fields such as those of thunder-clouds, *Proc. Cambridge Phil. Soc. 22*, 534–538.

Xu, W., S. Celestin, and V. Pasko (2012), Source altitudes of terrestrial gamma-ray flashes produced by lightning leaders, *Geophys. Res. Lett.*, *39*, L08801, doi:10.1029/2012GL051351.